

Reactivity of transition-metal alloys to oxygen and sulphur

Rajarshi Tiwari and James Nelson

School of Physics, AMBER and CRANN Institute, Trinity College Dublin, Dublin 2, Ireland

Chen Xu

Nokia Bell Labs, 600 Mountain Avenue, Murray Hill, NJ, USA

Stefano Sanvito

School of Physics, AMBER and CRANN Institute, Trinity College Dublin, Dublin 2, Ireland.

(Dated: April 30, 2020)

Oxidation and tarnishing are the two most common initial steps in the corrosive process of metals at ambient conditions. These are always initiated with O and S binding to a metallic surface, so that one can use the binding energy as a rough proxy for the metal reactivity. With this in mind, we present a systematic study of the binding energy of O and S across the entire transition-metals composition space, namely we explore the binding energy of **88** single-phase transition metals and of **646** transition-metal binary alloys. The analysis is performed by defining a suitable descriptor for the binding energy. This is here obtained by fitting several schemes, based on the original Newns-Anderson model, against density-functional-theory data for the *4d* transition metal series. Such descriptor is then applied to a vast database of electronic structures of transition-metal alloys, for which we are able to predict the range of binding energies across both the compositional and the structural space. Finally, we extend our analysis to ternary transition-metal alloys and identify the most resilient compounds to O and S binding.

I. INTRODUCTION

The electronic industry uses a wide palette of metals in various forms. Tiny metallic wires form interconnectors in logic circuits, thin magnetic films are the media in data storage, mesoscopic layers are found as solders and protective finishings in printed circuit boards. All these metals undergo corrosion processes, which can lead to degradation and ultimately to failure. In the last few years the problem has aggravated because of the increased multiplicity of the elements used, the reduced spacing between the various components, the often unpredictable users' environment and the deterioration of the air quality in region with a high level of industrial activity. Thus, it is desirable to identify classes of metallic alloys, which are particular resilient to corrosion and, at the same time, can deliver the functionality desired by the given application.

There are several known mechanisms of corrosion depending on the environmental conditions, such as the mixture of corrosive agents at play and the humidity level, but a full experimental determination of the dynamics of corrosion is often difficult to achieve. In general, a corrosive reaction is initiated by the binding of a chemical agent to a metallic surface, followed by the formation of a new phase, with or without the possible release of new molecules incorporating atoms from the metallic surface (mass loss). The progression of the corrosive reaction beyond the formation of a few reacted atomic layers is then determined by the diffusion of the corrosive agent in the metal and the self-diffusion of the metallic ions. At the macroscopic level, such mass transport mechanisms are further determined by the microstructure of the given sample, for instance through

diffusion at grain boundaries.

Given the general complexity of the corrosion process modelling studies must extend across different length and time scales¹. These studies usually provide a valid contribution to the understanding of the corrosion dynamics in a given material. The multiscale approach, however, is not suitable for scanning across materials libraries in the search for the ideal compound resisting corrosion in a known environment, since the numerical overheads and workflows are computational prohibitive and often require information from experiments (e.g. the microstructure). Thus, if one wants to determine a simple set of rules to navigate the large chemical and structural space of metallic alloys, the attention has to focus on one of the steps encountered in the corrosion path. A natural choice is that of determining the ease with which the first step takes place, namely to evaluate the reactivity of a given metal to a particular chemical agent.

This is precisely the approach adopted here, where we estimate the reactivity of a vast database of metallic alloys to both O and S. Oxygen and sulphur are particularly relevant, since for many metallic surfaces oxidation and tarnishing initiate the corrosion process at the ambient conditions where one typically finds electronic equipment. However, even the simulation of oxidation and tarnishing is complex and not amenable to a high throughput study. This, in fact, involves determining the full reaction path through an extensive scan of the potential energy surface or through molecular dynamics. As such here we take a simplified approach by computing the oxygen and sulphur binding energy to metals and by taking such binding energy as a proxy for reactivity. Clearly this is a drastic simplification, since sometime a material presents a similar binding energy to O and S but different

reactivity, as in the case of silver². Such situations typically occur when the rate-limiting barrier in the reaction path does not correlate well with the binding energy of the reaction product (see discussion in section III C), or when the interaction between the reactants on the surface changes the thermodynamics of the reaction as the coverage increases. However, the binding energy still provides a measure of the tendency of O and S to attack the surface, and it strongly correlates to the stability of the product oxide/sulphide phases (see later). As such it is a valuable quantity to classify metallic alloys as either weak or robust to corrosion.

Our computational scheme achieves the desired throughput by combining density functional theory (DFT) calculations with an appropriate *descriptor*³. In particular we use details of the density of state (DOS), namely the shape of the partial DOS (PDOS) associated to the transition metal *d*-bands, to construct a model that provides an estimate of the binding energy between a given metal alloy and both O and S. This is based on the notion that the O-metal and S-metal bonds get weaker as the metal *d* band is progressively filled⁴. Our strategy then proceeds as follows. We first fit the parameter of the model to DFT binding energy data for the 4*d* transition metal series. This is preferred to the 3*d* one, since it does not present elemental phases with magnetic order, and to the 5*d*, since the electronic structure can be computed without considering spin-orbit interaction. In particular, we explore several variations of the model and assess their ability to fit the data. Then, we construct an automatic workflow to extract the DOS information from the AFLOWLIB.org materials database⁵. This involves fitting the various orbital-resolved PDOS to a semi-elliptical DOS. Finally, we use the descriptor to compute the binding energy for all the experimentally known binary and ternary transition-metal alloys contained simultaneously in both AFLOWLIB.org and the Inorganic Crystal Structure Database (ICSD)⁶.

The paper is organized as follows. In the next section we introduce our methodology, by discussing the various descriptors considered, their rationale, the computed DFT data and the scheme for extracting data from AFLOWLIB.org. Next we present the descriptor fitting procedure and evaluate its error in determining the binding energy, before proceeding to show our results. We first determine the binding energy of O and S to transition-metal binary alloys and then we move to a restricted number of ternaries. Then we conclude.

II. METHODS

A. Rationale for the descriptors

The main idea beyond the definition of a descriptor is that it should represent a simple relation between a physical observable and a property of the electronic structure easy to calculate. Once this is established, the descriptor

can be used to scan large databases in the search for particular compounds of interest. In our case an insight on how to construct a descriptor for the binding energy between O/S and a transition metal alloy can be obtained by looking at Fig. 1. In the figure we report the experimental enthalpy of formation per atom, $-\Delta H_f$, for a wide range of oxides and sulphides across the 3*d*, 4*d* and 5*d* transition-metal series (the data used for constructing Fig. 1 are listed in the appendix together with their associated references), where multiple data corresponding to the same transition metal indicate that oxides/sulphides with different stoichiometry exist for that metal.

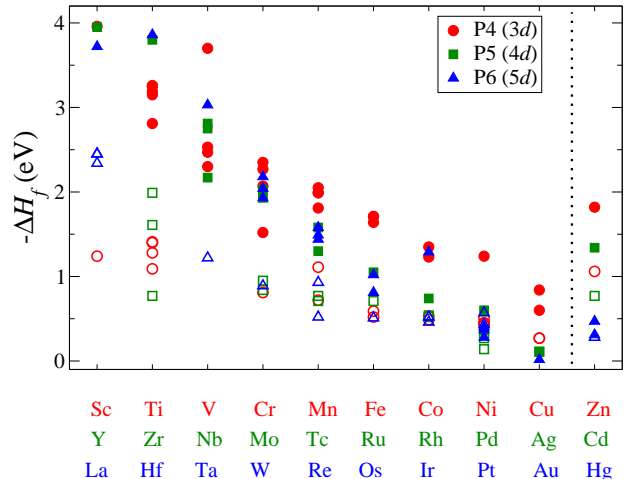


FIG. 1. (Color online) Experimental enthalpy of formation per atom for transition-metal oxides and sulphides across the 3*d* (red circles), 4*d* (green squares) and 5*d* (blue triangles) series. Open symbols are for sulphides and closed symbols for oxides. Multiple symbols for the same transition metal correspond to oxides/sulphides with different stoichiometry. For instance, there are five different data points for Ti-O, respectively TiO, Ti₂O₃, Ti₃O₅ and TiO₂ (both anatase and rutile). Note that for several transition metals additional stable phases exist, but they are not reported in the figure because their enthalpy of formation is not available (e.g. for Ti-O there also exist Ti₆O, Ti₃O, Ti₂O, and Ti₃O₂).

The figure reveals a number of clear trends. Firstly, we note that on average the enthalpies of formation of oxides are significantly larger than those of sulphides, owing to the fact that the electronegativity of O is larger than that of S. Secondly, for both oxides and sulphides the absolute value of the enthalpy of formation reduces monotonically (becomes less negative) across the transition-metal series. The slope of such reduction is significantly more pronounced for oxides than for sulphides, so that towards the end of the series $-\Delta H_f$ is very similar for these two groups ($-\Delta H_f$ for Ag₂O is almost identical to that of Ag₂S, ~ 0.11 eV/fu - fu = formula unit). Finally, the enthalpy of formation increases again beyond the noble metals (Cu, Ag and Au).

Importantly, these trends have not been observed only for the enthalpy of formation but also for the binding en-

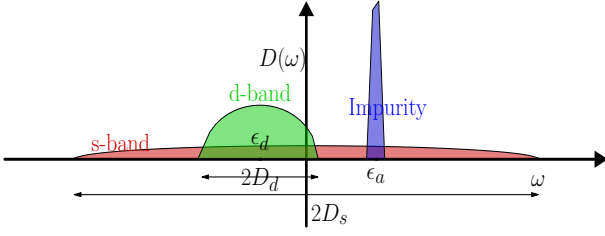


FIG. 2. (Color online) Level scheme showing the DOS for the Anderson impurity model. The s - p band of the metal is wide and the Fermi level is placed approximately at half filling. In contrast, the d band has a moderate width and it is centered at ϵ_d . The impurity level, whose width is determined only by the interaction with the metal, is at an energy, ϵ_a .

ergy of transition metals with monovalent atoms^{4,7} (e.g. H), with oxygen⁸ and with a broad range of molecular adsorbates^{9,10}. This suggests the formulation of a descriptor, characteristic of each adsorbate, based solely on the details of the electronic structure of the metal⁴. The crucial observation is that in typical transition metals the DOS is dominated by a partially filled, extremely broad s - p band, and by a relatively narrow d band. As the atomic number increases the occupation of the s - p band changes little, while the d band becomes progressively more filled, and hence moves to lower energies (with respect to the Fermi energy, E_F). Upon approaching the surface, the energy level of the adsorbate relevant for the bonding [in the case of O (S) the $2p$ ($3p$) shell] gets broadened by the interaction with the s - p band. At the same time, it forms a bonding and anti-bonding pair with the d band of the metal, which is here approximated as a single molecular level. Thus, at the beginning of the transition-metal series one has the situation in which the bonding level is filled and the anti-bonding one is empty, so that the binding energy is high. However, as the d band fills also the occupation of anti-bonding level increases, the adsorbate-metal bond weakens and the binding energy reduces.

It is then clear that the energy position of the d band of the transition metal, together with some measure of the strength of the transition-metal/adsorbate hopping parameter, can define a valuable descriptor for the binding energy. Two classes of such descriptors are defined in the next section.

B. Definition of the descriptors

We model oxygen and sulfur as a single impurity level coupled to a bath of electrons characterising the metal. The level of description for such bath defines the different models. The simplest one is often called the Newns-Anderson (NA) model¹¹, and it is defined by the following Hamiltonian,

$$H_{\text{NA}} = \epsilon_d d^\dagger d + \epsilon_a a^\dagger a + V_{ad}(a^\dagger d + d^\dagger a). \quad (1)$$

Here a^\dagger (a) and d^\dagger (d) are the creation (annihilation) operators, respectively, for the adsorbate and the metal d band, while ϵ_a and ϵ_d are the corresponding energy levels (before binding), and V_{ad} their hybridization (hopping integral). At this level the metal d band is treated as dispersionless and the contribution from the s - p band to the bond is neglected. H_{NA} can be easily diagonalised to yield the eigenvalues $\epsilon_\pm = \epsilon_a + \frac{1}{2}(\Delta_{ad} \pm W_{ad})$, where, $\Delta_{ad} = \epsilon_d - \epsilon_a$ and $W_{ad} = \sqrt{4V_{ad}^2 + \Delta_{ad}^2}$. If the fractional occupation of the d band is f , then the total energies before ($V_{ad} = 0$) and after ($V_{ad} \neq 0$) the coupling are $E_1 = 2(f\epsilon_d + \epsilon_a)$ and $E_2 = 2(1 + f)\epsilon_-$, respectively. Thus, the binding energy is given by

$$E_b = E_2 - E_1 = -(1 - f)(W_{ad} - \Delta_{ad}). \quad (2)$$

Finally, one can assume that there is an additional contribution to the binding energy, E_{sp} , originating from the interaction with the s - p band. Such contribution, however, is not expected to vary much across the transition-metal series so that it can be kept constant. The NA model, thus depends on four parameters. Two of them are associated respectively, to the metal, ϵ_d , and the adsorbate, ϵ_a , alone, one to the interaction between the two, V_{ad} , and one is a constant, E_{sp} , specific of each adsorbate. Note that when extracting the various parameters from electronic structure theory calculations (see next section), where the d band has dispersion, the d -band energy level, ϵ_d , is replaced by the position of the band center.

A more detailed description of the electrons in the metal is provided by the Anderson impurity model,¹² which is schematically illustrated in Fig. 2. In this case the metal band structure is taken into consideration through the Hamiltonian,

$$H_A = \epsilon_a a^\dagger a + \sum_{\mathbf{k}} \left(\epsilon_{\mathbf{k}}^s s_{\mathbf{k}}^\dagger s_{\mathbf{k}} + \epsilon_{\mathbf{k}}^d d_{\mathbf{k}}^\dagger d_{\mathbf{k}} \right) + \sum_{\mathbf{k}} (V_{\mathbf{k}}^s a^\dagger s_{\mathbf{k}} + V_{\mathbf{k}}^d a^\dagger d_{\mathbf{k}} + \text{h.c.}), \quad (3)$$

where now the operators $s_{\mathbf{k}}^\dagger(s_{\mathbf{k}})$ and $d_{\mathbf{k}}^\dagger(d_{\mathbf{k}})$ create (destroy) an electron with wave-number \mathbf{k} , respectively, in the s - p and in the d band. The band energies are $\epsilon_{\mathbf{k}}^s$ and $\epsilon_{\mathbf{k}}^d$ and the hopping parameters $V_{\mathbf{k}}^s$ and $V_{\mathbf{k}}^d$.

The model defined by Eq. (3) can be solved by constructing the appropriate Green's function, as shown in detail in Appendix A. In brief, the 'impurity' Green's function can be written as

$$G_{aa}(\omega) = \frac{1}{\omega - \epsilon_a - \Sigma(\omega)}, \quad (4)$$

where $\Sigma(\omega)$ is the self energy describing the interaction with the metal. This is given by

$$\Sigma(\omega) = \sum_{\mathbf{k}} \left(\frac{|V_{\mathbf{k}}^d|^2}{\omega - \epsilon_{\mathbf{k}}^d + i\eta} + \frac{|V_{\mathbf{k}}^s|^2}{\omega - \epsilon_{\mathbf{k}}^s + i\eta} \right), \quad (5)$$

with $\eta \rightarrow 0^+$. If we assume that the couplings are independent of \mathbf{k} , namely $V_{\mathbf{k}}^d = V_d$ and $V_{\mathbf{k}}^s = V_s$, we can simplify the self energy into $\Sigma(\omega) = \Lambda(\omega) - i\pi\Delta(\omega)$, so that the DOS, $D_a(\omega) = -\frac{1}{\pi}\text{Im}[G_{aa}(\omega)]$, writes as

$$D_a(\omega) = \frac{\Delta(\omega)}{[\omega - \epsilon_a - \Lambda(\omega)]^2 + \pi^2\Delta(\omega)^2}. \quad (6)$$

Explicit expressions for the real, $\Lambda(\omega)$, and imaginary part, $\Delta(\omega)$, of the DOS are detailed in Appendix A. Finally, the binding energy can be obtained by integrating the DOS,

$$E_b = \int_{-\infty}^0 D_a(\omega)d\omega - \epsilon_a, \quad (7)$$

where all the energies are defined from the metal Fermi energy, $E_F = 0$.

As defined, the Anderson impurity model depends on the adsorbate energy level, the metal/adsorbate electronic coupling and the metal DOS. Here we approximate the metal DOS with a semi-circular model. In particular the d -band DOS, $D_d(\omega)$, is described as a semi-circle with center at ϵ_d and half bandwidth, w_d , namely as

$$D_d(\omega) = \frac{2}{\pi w_d} \sqrt{1 - \frac{(\omega - \epsilon_d)^2}{w_d^2}}. \quad (8)$$

In contrast the s - p band is taken as having its center at zero and a large bandwidth, w_s ,

$$D_s(\omega) = \frac{2}{\pi w_s} \sqrt{1 - \frac{\omega^2}{w_s^2}}. \quad (9)$$

Thus, in addition to ϵ_a and the relevant hybridisation parameters the Anderson model is uniquely defined by the center and width of the d band and by the width of the s - p one. Furthermore, since we take the approximation that the s - p band remains unchanged across the transition metal series its contribution to the integral of Eq. (7) can be simply replaced by a constant, E_{sp} , specific for each adsorbate.

In what follows the band parameters, ϵ_d and w_d , will be extracted from DFT calculations with a procedure described in the next sections, while ϵ_a and E_{sp} will be considered as fitting parameters. Finally, as far as V_{ad} is concerned, we will use a well-known strategy¹³ of considering the tabulated values extracted from the LMTO potential functions.¹⁴ These are essentially scaling rules, so that the hybridisation parameters are all known up-to a general scaling constant, β , which also will be fitted. Note that the same scaling rules are also used for the NA model, which then requires the parameter β . Note also that the band parameters, which in principle should be computed for each specific surface, are here replaced with those of the bulk compound. This is an approximation that allows us to perform a large-scale analysis of the entire transition metal space, but that makes our

Model	DFT				FIT		
NA	ϵ_d	V_{ad}			ϵ_a	E_{sp}	β
M1	ϵ_d	V_{ad}	w_d		ϵ_a	E_{sp}	β
M2	ϵ_d	V_{ad}	w_d	WF	$\epsilon_a + WF$	E_{sp}	β

TABLE I. The different models investigated in this work. Quantities indicated with ‘DFT’ are directly extracted from DFT calculations for bulk materials, while those in the ‘FIT’ column are taken as fitting parameters. Note that none of the models is defined by more than three fitting parameters, specific for each adsorbate.

model insensitive to the surface details. The validity of such approximation will be discussed in section III A.

A summary of the models investigated is presented in Table I, where we separate the quantities that we will extract from DFT (‘DFT’ column) from those used as fitting parameters (‘FIT’ column). NA is the original Newns-Anderson model, Eq. (2), with ϵ_d taken as the d -band center. In contrast, M1 and M2 are just numerically defined and essentially implement Eq. (7). In M1 the adsorbate energy level is constant for each adsorbate, while in M2 its position is shifted by the experimental work-function of the metal, WF (either experimental or extracted from DFT). Note that all the models require only three fitting parameters.

C. Density functional theory calculations

DFT calculations are performed for the $4d$ transition metal series (Y to Cd), which is taken as benchmark for our models and as training dataset for their fit. We use the all-electron FHI-AIMS code¹⁵, since its local-orbital basis set makes it more numerically efficient than plane-wave schemes in computing surfaces. A revised version of the Perdew-Burke-Ernzerhof (RPBE) exchange-correlation functional¹⁶, extensively tested for adsorption energies, is considered throughout this work, together with the ‘light’ basis-set FHI-AIMS default. Tests for the more accurate ‘tight’ basis set have revealed that the average error is minimal compared with that of the descriptor.

For all the $4d$ elemental phases we perform two sets of calculations either considering the experimental lattice structure (see table II) or a hypothetical *fcc* structure at the RPBE energy minimum. In both cases we construct 4-to-6-layer thick slabs with surfaces along the [100], [110] and [111] directions. The lateral dimensions of the supercell is such that the surface contains a minimum of 4 atoms, so to minimise the interactions between the periodic images (single impurity limit). The reciprocal space is sampled with a $12 \times 12 \times 1$ grid and the relaxation is converged when the forces are smaller than 5.0×10^{-3} eV/Å.

TABLE II. Summary table of the elementary phases of the 4d transition-metal series investigated in this work. For each element we report the atomic number, Z , the atomic configuration, the lattice structure of the thermodynamically stable phase at room temperature, the most stable surface (the one investigated here), the experimental work function, WF (in eV), the Pauling electronegativity, EN , (for O and S this is 3.44 and 2.58 respectively), the computed energy position of the d band (in eV), ϵ_d , the computed width of the d band, w_d (in eV). Note that ϵ_d is taken with respect to the Fermi level, which is set to zero.

El.	Z	Conf.	Lattice	Surface	WF	EN	ϵ_d	w_d
Y	39	$5s^2 4d^1$	hcp	(0001)	3.1	1.22	1.77	1.88
Zr	40	$5s^2 4d^2$	hcp	(0001)	4.05	1.33	1.12	2.14
Nb	41	$5s^2 4d^3$	bcc	(100)	3.95-4.87	1.60	0.31	2.12
Mo	42	$5s^2 4d^4$	bcc	(100)	4.36-4.95	2.16	-0.18	2.19
Tc	43	$5s^2 4d^5$	hcp	(0001)	5.01	1.9	-0.87	2.34
Ru	44	$5s^2 4d^6$	hcp	(0001)	4.71	2.2	-1.76	2.14
Rh	45	$5s^2 4d^7$	fcc	(100)	4.98	2.28	-1.98	1.76
Pd	46	$5s^2 4d^8$	fcc	(100)	5.22-5.6	2.2	-1.96	1.41
Ag	47	$5s^2 4d^9$	fcc	(100)	4.64	1.93	-4.3	0.90
Cd	48	$5s^2 4d^{10}$	hcp	(0001)	4.08	1.69	-8.95	0.45

The binding energy is then calculated as

$$E_b = E_{\text{ads+slab}} - E_{\text{slab}} - E_{\text{ads}} \quad (10)$$

where, E_{ads} is the DFT energy of the adsorbate alone (oxygen or sulfur) in its atomic form, E_{slab} that of the ‘relaxed’ slab, and $E_{\text{ads+slab}}$ is the energy of the relaxed slab including the adsorbate at its equilibrium position. We always relax the top layer of the slab when calculating either E_{slab} or $E_{\text{ads+slab}}$. In both cases the lower layers are kept fixed to reduce the computational overhead. The orbital-resolved DOS for the bulk structure and for the various surfaces are always calculated to be used for fitting the models. In that case the Brillouin zone is sampled with a $144 \times 144 \times 144$ and a $144 \times 144 \times 1$ grid, respectively.

D. Data extraction from AFLOWLIB.org

As explained before we have carried out novel RPBE-DFT calculations only for the 4d transition-metal series, which has served as dataset for fitting the model. Once the model has been determined this has been run over an existing extremely large dataset of electronic structure calculations. In particular we have extracted data from the AFLOWLIB.org library⁵. At present, this contains basic electronic structure information (DOS, band structure, etc.) for about 3.2 millions compounds, including about 1,600 binary systems ($\sim 350,000$ binary entries) and 30,000 ternary ones (2,400,000 ternary entries). These have all been computed at the PBE level with the DFT numerical implementation coded in the VASP package¹⁷, and with extremely standardised convergence criteria. In particular, a subset of the AFLOWLIB.org

data is for experimentally known compounds, namely for entries of ICSD.⁶ Our work investigates that particular subset.

It must be noted that there may be an apparent inconsistency in constructing the models by using RPBE electronic structures and applying them to PBE data. However, one has to consider that RPBE is a variation of PBE designed to improve over the energetics of chemisorption processes. The two functionals remain relatively similar, and most importantly here, they produce rather close Kohn-Sham spectra, and hence DOS. The variations in DOS between RPBE and PBE have very little influence on the determination of the binding energy from our models, and certainly they generate errors much smaller than that introduced by not considering structural information in our descriptors (see next section).

The AFLOWLIB.org library is accessible through a web-portal for interactive use, but most importantly through a RESTful Application Program Interface (API).¹⁸ This implements a query language with a syntax, where comma separated ‘keywords’ (the material properties available) are followed by a ‘regular expression’ to restrict the range or choice of the keywords. For instance the string “Egap(1*,*1.6),species(Al,O),catalog(icsd)” will give us a list of compounds containing Al and O and included in ICSD, whose band gap ranges in the interval [1eV, 1.6eV]. Such queries are submitted to the server <http://aflowlib.duke.edu/search/API/?>. Here we have used the AFLOWLIB.org RESTful API, together with Python scripting, to search and extract the material information of transition-metal (i) elemental phases, and both (ii) binary and (iii) ternary alloys. In all cases we have limited the search to metals only.

We have found that, in general, for a given material prototype AFLOWLIB.org contains multiple entries. Some correspond to different stable polymorphs, but also there is redundancy for a given lattice, where multiple entries differ by small variations of the lattice constants. These are typically associated to independent crystallographic characterisations of the same material, taken under slightly different experimental conditions (temperature, pressure, etc.) or at different moments in time. Such small variations typically change little the electronic structure, so that for our purpose they provide no extra information. We have then removed such ‘duplicates’ by grouping the compounds by lattice symmetry and total DFT energy. Then, for a given crystal structure we have selected the entry presenting the lowest energy. Such procedure has returned us 88 elemental phases, 646 binary and about 50 ternary metallic alloys. For these we have extracted the orbital-resolved DOS, which was then fitted to the semi-circular DOS of Eq. (8).

The fit proceeds by minimising the mean squared variance between the actual DFT-calculated DOS, $D_{\text{DFT}}(\omega)$, and the semicircular expression, $D_d(\omega, \epsilon_i, w_i)$, namely by

minimising the following quantity

$$\Delta D = \left(D_{\text{DFT}}(\omega) - \sum_{i=1}^n \eta_i D_d(\omega, \epsilon_i, w_i) \right)^2. \quad (11)$$

Here, n is the number of semicircles used in the fit, while η_i , ϵ_i , w_i are the weights, centres and half widths of each semicircle, respectively. We have initially used a variable number of semicircles to fit the DOS, but found that a single one for each atomic orbital was always providing the best result. The fit extends to all species present in a compound and all orbital channels (s , p , d and sometime f), but only data related to the d band, ϵ_d and w_d , of all the species are retained when using the model. An example of such fit is provided in Fig. 3 for Pt_2Y_1 .

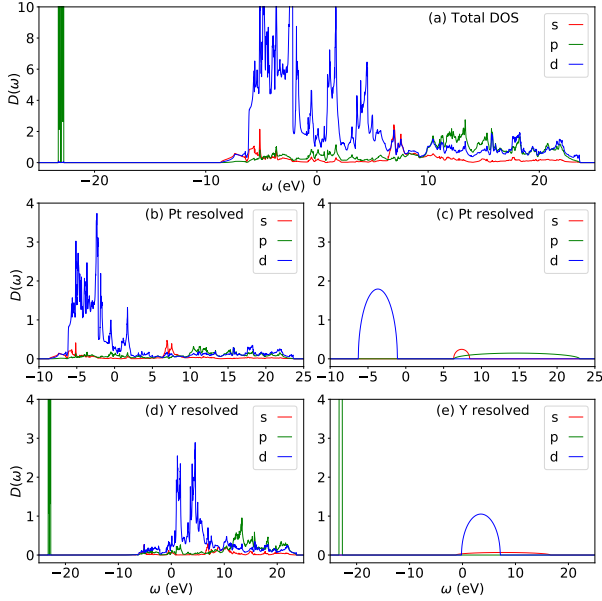


FIG. 3. (Color online): Orbital-resolved DOS for Pt_2Y_1 (ICSD 649861), as extracted from AFLOWLIB.org and its corresponding fits. In panel (a) we show the DFT-computed total orbital-resolved DOS. Panels (b) and (d), respectively are the element-resolved, orbital-resolved DOS for Pt and Y. In panels (c) and (e) we show our semi-circular fit to the Eq. (8) semicircular DOS.

III. RESULTS AND DISCUSSION

A. Fitting the models

Each of the three models introduced in the previous sections requires to determine three parameters, ϵ_a , β and E_{sp} , specific to each adsorbate. These are obtained by fitting the RPBE data for the 4d transition-metal series. In particular we minimise the sum of the mean squared difference between the DFT binding

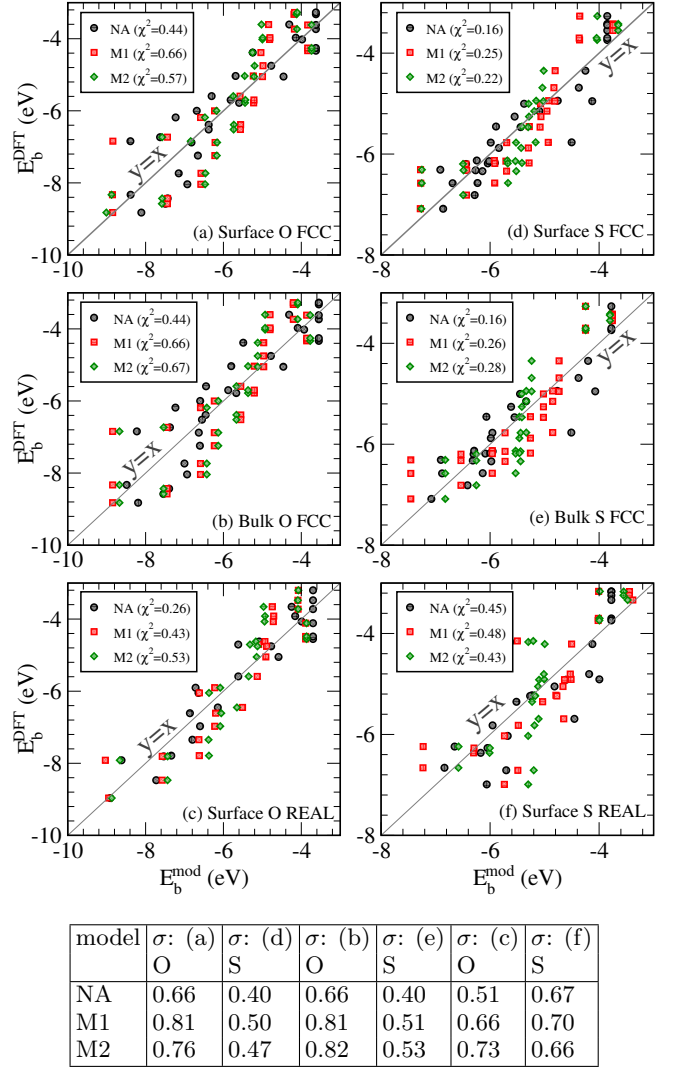


FIG. 4. (Color online) Comparison between the DFT binding energies and those estimated with the best fit of the various models. The left column [panels (a)-(c)] is for oxygen, while the right column [panel (d)-(f)] for sulfur. Circles, squares and diamonds correspond to the NA, M1 and M2 model, respectively. The relative χ^2 minimum of each model is shown in the legends (see text for details). The table contains the binding-energy mean deviation, $\sigma = \sqrt{\chi^2(\epsilon_a, \beta, E_{sp})}$. The two top panels are for the *fcc* structures with the fit done over the DOS of the specific surfaces; the two middle are again for the *fcc* structures, but now we use the bulk DOS for the fit; the two lower panels are for the actual experimental crystal structures of the compounds.

energies, E_b^{DFT} , and those computed by the models, $E_b^{\text{mod}}(\epsilon_a, \beta, E_{sp})$, namely

$$\chi^2(\epsilon_a, \beta, E_{sp}) = \frac{1}{N_s} \sum_{i \in [\text{Y-Cd}]} [(E_b^{\text{DFT}})_i - E_b^{\text{mod}}(\epsilon_a, \beta, E_{sp})_i]^2. \quad (12)$$

where N_s is the total number of surfaces taken over the [Y-Cd] range. For *fcc* bulk and surface, $N_s = 33$, while

for real structures we had $N_s = 28$. The fits for O and S are performed independently, with ϵ_d taken from the RPBE calculations, V_{ad} from the scaling laws of Ref. [14] and WF from experiments. Finally, the electronic filling of the d band, f , or equivalently the position of the Fermi energy are also taken from the RPBE calculations.

Our best fits are presented in Fig. 4, where we show the model-predicted energies against the RPBE values for both oxygen [panels (a)-(c)] and sulfur [panels (d)-(f)]. The table below the figure reports the mean absolute deviation of the binding energy, $\sigma = \sqrt{\chi^2(\epsilon_a, \beta, E_{sp})}$. As we go down the rows in the figure, we have three different sets of fit, which differ for the choice of the DFT-calculated DOS taken to compute the d -band centre and bandwidth, and for the target DFT energies. In the first row [panels (a) and (d)] the DOS is that of the surface atoms of the metals constrained to the *fcc* lattice, and so are the target DFT energies. In the second-row panels [(b) and (e)] the DOS is that of the bulk *fcc* lattice, while the target binding energies remain the same. Finally the last panels [(c) and (f)] use data for the metals in their thermodynamically stable structure (see Table II).

In general we find that all the models tend to perform better for oxygen than for sulphur, in particular when the actual equilibrium structures are considered [panels (c) and (f)]. Note that the spread of the DFT RPBE binding energies for O is significantly larger than that of S (by about 2 eV), reflecting the same trend observed for the enthalpies of formation of oxides and sulphides (see Fig. 1). This means that a similar χ^2 translates in a smaller relative error for O. Interestingly, while in the case of O our best fit is obtained for the experimental structures, the opposite happens for S, for which the fit for the hypothetical *fcc* lattice is significantly more accurate. In fact, we find that the worst performance is obtained for S and the experimental structures, regardless of the model used. This large error is associated to a significant scattering in the actual DFT data, in particular towards the beginning of the series. For instance we find that when going from the most stable (0001) surface of *hcp* Y to the same for Zr the binding energy marginally increases (becomes less negative), as expected from the larger occupation of the d band. However, when moving to the most stable (100) surface of *bcc* Zr, E_b significantly decreases and in fact it becomes lower than that of both Y and Zr. Clearly such behaviour cannot be captured by any of the models, since when going from Y to Zr to Nb the position of ϵ_d monotonically increases (see Table II). Similar anomalies are found for Ru and Rh, although much less pronounced.

The much more pronounced spread in binding energies for sulphur can be attributed to its electronegativity, lower than that of oxygen, and to the associated ability to form compounds involving transition metals over a broad range of stoichiometry. This is particularly evident towards the beginning of the transition metal series. For instance, while Y forms only one stable oxide and one sulphide, Y_2O_3 and Y_2S_3 , so that it takes only the

3+ oxidation state, Zr has a single oxide, ZrO_2 , but can form sulphides with five different stoichiometries, ranging from Zr_3S_2 to ZrS_3 (see tables in Appendix D). Most importantly the enthalpy of formation of these different sulphides varies significantly, from 0.77 eV/atom for Zr_3S_2 to 1.99 eV/atom for ZrS_2 . It is also interesting to note that even when there are stable oxides formed with the same transition metal but with different stoichiometry, therefore yielding a different oxidation state for the metal, the fluctuation in enthalpy of formation remains small. For instance one can find NbO (Nb oxidation state 2+) with an enthalpy of formation of 2.17 eV/atom and Nb_2O_5 (Nb oxidation state 5+) with an enthalpy of formation of 2.81 eV/atom.

A second important conclusion can be taken by looking at the first two rows of Fig. 4, where the same DFT binding energies computed for the *fcc* lattice are modelled by using the band parameters of either the surface atoms [panels (a) and (d)] or those of the bulk [panels (b) and (e)]. Clearly the two sets of fit present very similar errors, a fact that reflects the small changes in band parameters when going from the surface to the bulk. Indeed such changes do exist and in fact there is established evidence for binding energy shifts with d -band center shifts.¹⁹ However, while the inclusion of these small corrections improve the fit when a relatively narrow range of metals is considered, they have little impact in our case, that considers the entire transition metal series. Since our intention is to examine a very broad range of metallic alloys we can approximate the DOS of the surface with that of the bulk. This allows us to avoid performing surface calculations for the several hundreds compounds previously selected. An interesting possibility for improving on such assumption would be that of constructing a simple descriptor correlating the DOS narrowing at surfaces with the DOS of the bulk.

A more quantitative estimate of the accuracy of our model, at least for the elemental phases, can be obtained by analysing in more detail the distribution of DFT binding energies for the 4*d* transition-metal series across the different surfaces of the actual structures and the hypothetical *fcc* ones. Such distribution is available in Fig. 4, and it is re-plotted as a function of the atomic number in Fig. 10 in appendix B. From the figures we notice that the spread in values is of the order of 1 eV across the series, with the exception of Tc and both Mo and Nb, but only in the case of S. Clearly, Tc is not a matter of concern, since it is radioactive and forms a rather limited number of known binaries. Mo and Nb are more problematic and effectively set the accuracy of our model, which is of the order of ± 1 eV.

Finally, we notice that when comparing the different models we find little difference in accuracy, with the original NA model performing slightly better than both M1 and M2. This fact is somehow counterintuitive, since one expects a better fit for models including more parameters. We attribute such behaviour to the fact that here we apply the models to a very broad distribution of bind-

ing energies, for which the fluctuations of the DFT values are relatively large. Over such range the accuracy of the model is mainly driven by the d -band center, while finer details, such as the bandwidth, appear to have little impact. Note that in literature there are several examples of model improvements associated to descriptors, which include more information about the band shape²⁰. These, however, are related to narrow subsets of compounds, for which the d band center changes little, and the binding energy is driven by more subtle features of the electronic structure. For this reason in the remaining of the paper we will consider the NA model only.

B. Binding energies of binary alloys to O and S

We now discuss the trends in reactivity of transition-metal binary alloys to oxygen and sulfur. Out of the 30 transition metals there are $30 \times 29/2 = 435$ binary systems, a number that needs to be compared with the 646 binary intermetallic compounds found at the interception between the AFLOWLIB.org and the ICSD databases. A more detailed view of the chemical distribution of such 646 compounds can be obtained by looking at Fig. 5, where we graphically plot the number of stable phases for each of the 435 binary systems. Firstly, we note that there are several binary systems for which no single compound is found. This does not necessarily mean that the two elements are not miscible, but simply that there is no stable ordered crystalline phase, for which a full crystallographic characterisation is available. This is, for instance, the case of the Hf-Zr system; the two elements are miscible at any concentration, but the thermodynamically stable phase is a solid-state solution across the entire composition diagram. A similar situation is found for many binary systems made of elements belonging to the same group or to adjacent groups, namely along the right-going diagonal of the matrix of Fig. 5. In contrast, there is a much stronger tendency to form stable intermetallic phases in binary systems comprising an early ($d^0 - d^3$) and a late ($d^7 - d^{10}$) transition metal. For instance Ti-Pd is the system presenting the largest number, namely 12 of stable phases.

Next we move to discuss the trend in binding energies to oxygen and sulfur across the binary-system space. Clearly the binding energy is an object that depends on both the chemical composition and the stoichiometry of a compound, namely for a binary alloy it is a four dimensional function. Thus for the A_xB_y binary one has $E_b(A_xB_y) = f(A, x, B, y)$. We then proceed in the following way. For each binary system $A-B$ we analyse all existing stoichiometry, A_xB_y , and compute all the possible binding energies by running the NA descriptor against the partial DOS of all inequivalent bulk atomic sites. Then, we plot on a matrix analogous to that of Fig. 5 the minimum, E_b^{\min} , and maximum, E_b^{\max} , binding energy found for that system, namely

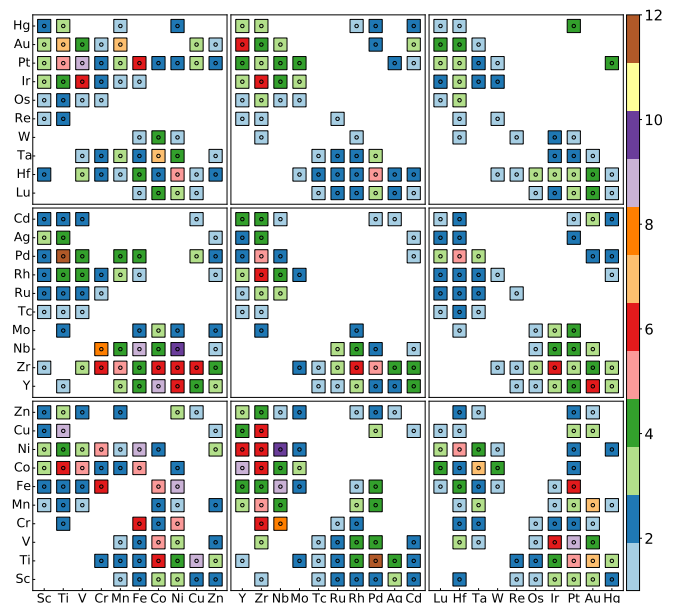


FIG. 5. (Colour online): Distribution of stable phases across the entire transition-metal binary system map. The number of compounds for a given binary system is colour coded.

$$E_b^{\max}(A : B) = \max_{x,y} \{E_b(A_xB_y)\}, \quad (13)$$

$$E_b^{\min}(A : B) = \min_{x,y} \{E_b(A_xB_y)\}. \quad (14)$$

The results of this analysis for both oxygen (left-hand side graph) and sulphur (right-hand side graph) are presented in Fig. 6, where E_b^{\min} and E_b^{\max} occupy the two halves of a circle and are encoded as a heat map. In the figure red tones indicate a weak binding energy, thus low reactivity, while the green/blue ones are for strong binding and high reactivity. When the two halves of a particular circle appear approximately of the same colour there is little variance in binding energy across stoichiometry and binding sites, while a strong contrast means that for that binary system there are extremely reactive sites (for some stoichiometry) together with weak ones (for the same compound or for different ones). Note that Fig. 6 just depicts the trend in reactivity, but it cannot be taken as an absolute measure of the binding energy across the binary space. In fact, it is not guaranteed that either E_b^{\min} or E_b^{\max} are actually accessible. For instance one may have the situation in which the most reactive site of a given binary system is associated to an unstable surface, so that it will be hardly available in practice.

Nevertheless, Fig. 6 provides valuable insights into the reactivity to oxygen and sulfur of the transition-metal alloys. As expected one finds the less reactive compounds among the alloys made of late ($d^7 - d^{10}$) transition metals, regardless of the period they belong to. For these the binding energy is small and so is the variance across stoichiometry and binding sites. The binding energy then becomes increasingly more negative as we move along the

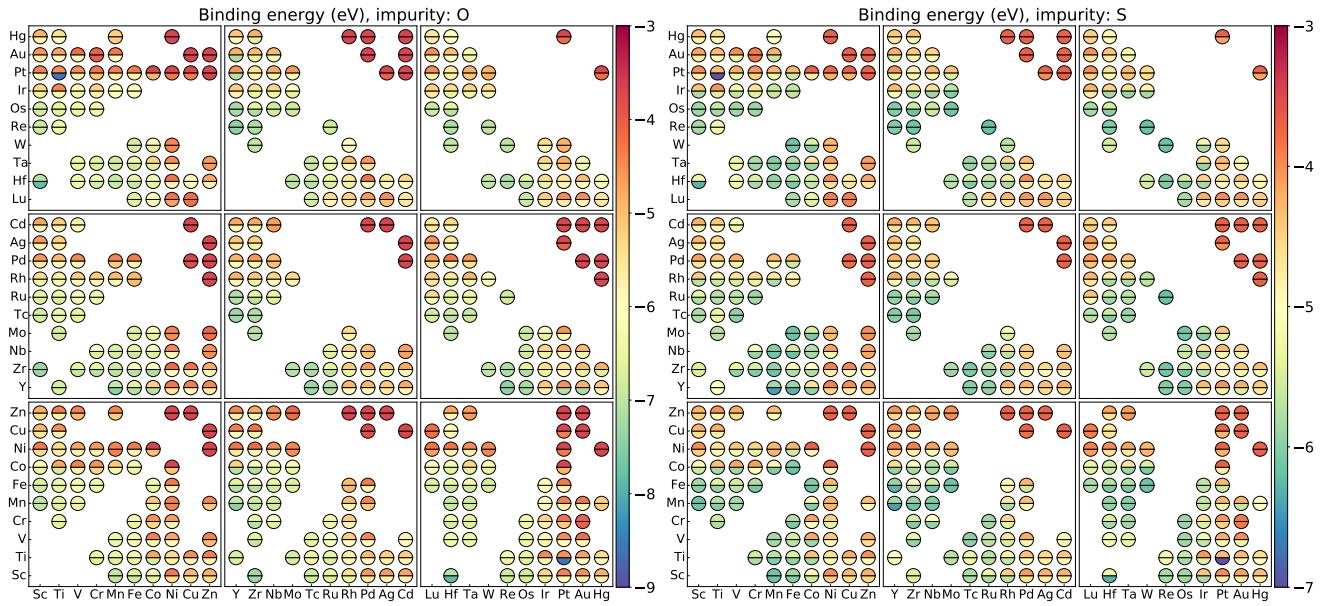


FIG. 6. (Colour online) Binding-energy map across the transition-metal binary systems. The left panel is for oxygen, and right panel for sulfur. For each given binary the colour of the two semicircles encodes the value of E_b^{\min} and E_b^{\max} (energies are in eV according to the heat-map scale depicted on the side of each picture). These are taken across the different stoichiometry and possible binding sites for any given binary system.

diagonal of the plots towards early ($d^0 - d^3$) transition metals. For this class the variance still remains relatively low owing to the fact that the position of the center of the d band is similar for elements in near groups. A different situation is encountered when one moves off the plot diagonal, namely towards alloys combining an early and a late transition metal. In this case we typically find both strongly and weakly reactive sites. An extreme example is found for the Pt-Ti system, where an E_b^{\min} of -8.62 eV is found for the Ti site of Ti_3Pt_1 , while a E_b^{\max} of -4.53 eV corresponds to Pt in Ti_1Pt_8 . This last group is of particular interest, in particular if one can find binary alloys with an overall weak reactivity, since the constituent elements do not include only expensive noble metals. It is also important to note that there is correlation in the variance between E_b^{\min} and E_b^{\max} and the abundance of compounds in a particular binary system (see Fig. 5). In fact, we find that more abundant binary systems, which have potentially a larger stoichiometric space (and thus a larger variance in possible inequivalent binding sites), have a larger colour contrast in Fig. 6.

Let us now compare the two panels of Fig. 6 for oxygen and sulphur. This is an important exercise, since often in an ambient-condition corrosion process O and S compete for the same binding site, thus that their relative reactivities may determine the final products of reaction and the overall reaction rate. In general, a bird-eye view of the data suggests rather similar qualitative chemical trends for sulphur and oxygen. However, a closer look reveals a few differences: (i) the overall binding energies for sulphur are lower than those of oxygen (note that

the scales in the two panels of Fig. 6 are different); (ii) the spread, or the variation over the minima and maxima (basically the colour contrast between the upper and lower semi-circles), for sulphur is typically larger than for oxygen (e.g. in Hg:Pt).

C. Reactivity of binary alloys to elemental O and S

We are now going to develop a simple criterion for estimating, on a more qualitative ground, the relative reactivity of a given binary system to S and O. The idea is to compare the predicted reaction rates for O and S absorption and to evaluate these from our computed binding energies. For simplicity here we take O_2 and S_2 as the main reactants, so that the reaction of interest is: $TM + 1/2O_2 \rightarrow TM_O$, where TM indicate the transition metal and TM_O the transition metal with one O adsorbed (the same holds for S). The enthalpy of reaction, δE^n ($n = O, S$), can then be simply written as $\delta E^n = E_b^n + 1/2E_{atom}^{n_2}$, where $E_{atom}^{n_2}$ is the experimental atomization enthalpy for either O_2 (5.1 eV) or S_2 (4.4 eV), and E_b^n is the binding energy of the n specie. Importantly, the enthalpy of reaction is often found to be linearly correlated to the activation energy, at least in the case of small molecules interacting with late transition metals. These so-called Brønsted-Evans-Polanyi relations^{21,22} thus establish a simple connection between a thermodynamical quantity, the enthalpy of reaction, and a dynamical one, the activation energy, E_{act}^n . Thus, one has $E_{act}^n = \gamma \delta E^n + \xi$, where the coefficients γ and ξ are, in

principle, specific of any given reactant. Finally, the reaction rate, κ , is solely determined by the activation energy via the usual Arrhenius expression, $\kappa = \nu e^{-E_{\text{act}}/k_B T}$, where ν is the frequency factor, T the temperature and k_B the Boltzmann constant.

The crucial point in the discussion is the observation that the scaling coefficient entering the Brønsted-Evans-Polanyi relations, γ and ξ , are universal for different classes of molecules and/or bonds^{23,24}. For instance for simple diatomic homonuclear molecules (e.g. O_2 , N_2) one finds $\gamma \sim 0.95$ and $\xi \sim 2$ eV. By assuming that the same relation is valid also for S_2 , we can then write an expression for the ratio between the reaction rates of O and S, namely

$$\frac{\kappa_S}{\kappa_O} = \frac{\nu_S}{\nu_O} \exp\left(-\frac{\gamma(\delta E^S - \delta E^O)}{k_B T}\right). \quad (15)$$

If one wants to use Eq. (15) to determine the relative reaction rate at ambient conditions, then we will write $T = 300$ K, and a further simplification can be made by assuming that the frequency factors for O_2 and S_2 are similar, $\nu_S/\nu_O \sim 1$. Finally, considering that the typical S concentration in the lower atmosphere is about 1 ppm, one expects similar corrosion to S and O when their reaction rates are in the ratio $\kappa_S/\kappa_O \sim 10^6$. This leads to the condition

$$1 = \frac{1}{2} \exp\left(-\frac{\gamma(E_b^S - E_b^O)}{0.025 \text{ eV}}\right). \quad (16)$$

We can then conclude that a given transition metal alloy will corrode equally to S and O when $E_b^S \sim E_b^O$, otherwise the reactivity will be dominated by oxidation.

It is important to note, however, that in the atmosphere S is present mainly in the SO_2 and H_2S form, and not as S_2 . Unfortunately Brønsted-Evans-Polanyi relations are currently unavailable for SO_2 and H_2S so that a more quantitative analysis of the ambient relative reactivity of O and S cannot be carried out. Nevertheless, the ratio κ_S/κ_O of Eq. (15) can serve as a useful descriptor to analyse the relative reactivity to S and O of a binary system. This analysis is carried out in Fig. 7, where we plot $\ln(\kappa_S/\kappa_O)$ over our binary space, and we take E_b^{max} as binding energy.

As expected the $\ln(\kappa_S/\kappa_O)$ map closely resembles that of the binding energies (see Fig. 6), with lower κ_S/κ_O ratios for the late transition metals (particularly in the 5d period), while the reactivity to O is always largely dominant. From the figure it is clear that the condition $\kappa_S/\kappa_O > 10^{-6}$, which makes the ambient corrosion to S stronger than that to O, is met only for a rather limited number of binary systems. In fact, this seems to be unique to alloys with both atomic species having more than 10 valence electrons (Ni, Pd and Pt). However, it is important to note that this analysis is based on E_b^{max} , so that it is not specific of a particular compound, but simply explore trends in the binary space. One can then still have binary compounds, where the electronic interplay between the atomic species results in lower binding

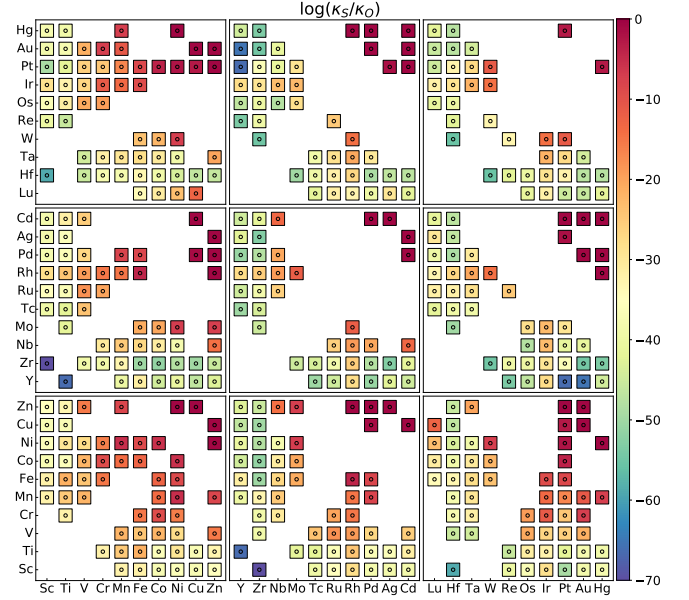


FIG. 7. (Colour online): Reaction rates ratio κ_S/κ_O , Eq. (15), for the binary systems investigated. Here $\ln(\kappa_S/\kappa_O)$ is plotted as a heat map for all the binary compositions by taking as binding energy E_b^{max} .

energies, and therefore reactivity, with respect to the binary system they belong to. This analysis is carried out next.

D. Reactivity gain for binary compounds

Our task here is to identify those binary compounds, in which the binding energy of the different inequivalent sites differs the most from that of the corresponding single-element phases. In other words we wish to find those binary alloys for which the bond formation between chemically different atoms alters the most the position of the d band with respect to that of the elemental phase. For a generic $A_x B_y$ binary alloy such property can be captured by the “elemental energy shift”, a descriptor defined as

$$\Delta E_{\text{el}} = E_b^n - E_{\text{el}}^n, \quad (17)$$

where E_b^n is the binding energy for the species n ($n = A, B$) in the binary alloy and E_{el}^n is the binding energy of the elemental phase of n . In particular, for any binary compound we compute the maximum and minimum value of ΔE_{el} . Here $\Delta E_{\text{el}}^{\text{max}}$ (typically a positive value) corresponds to the particular site whose binding energy has been increased the most in forming the alloy (the site is less reactive than the same element in its elemental phase), while $\Delta E_{\text{el}}^{\text{min}}$ (typically a negative value) is for the site whose binding energy has been reduced the most (the site is more reactive than in its elemental phase). These two quantities are listed in Table III

for the 24 compounds presenting the largest $\Delta E_{\text{el}}^{\text{max}}$ and $\Delta E_{\text{el}}^{\text{min}}$ for both O and S. In the same table we also list the composition-averaged binding energy, \tilde{E}_{b} , defined as $\tilde{E}_{\text{b}} = w_x E_{\text{b}}^{\text{A}} + w_y E_{\text{b}}^{\text{B}}$, where $w_x = x/(x+y)$ [$w_y = y/(x+y)$]. This latter energy provides a rough estimate of the global reactivity of a particular compound.

TABLE III. List of the binary compounds possessing binding sites, whose binding energy present large deviations with respect to that of their corresponding elemental phases. All energies are in eV. In the brackets we report the particular element associated to ΔE_{el} .

Comp	Oxygen			Sulphur		
	\tilde{E}_{b}	$\Delta E_{\text{el}}^{\text{max}}$	$\Delta E_{\text{el}}^{\text{min}}$	\tilde{E}_{b}	$\Delta E_{\text{el}}^{\text{max}}$	$\Delta E_{\text{el}}^{\text{min}}$
RhY	-5.87	4.44 (Y)	-3.18 (Rh)	-4.63	2.01 (Y)	-0.83 (Rh)
Cu ₅ Y	-4.38	4.44 (Y)	-4.08 (Cu)	-3.99	2.01 (Y)	-1.76 (Cu)
Ir ₂ Y	-5.14	4.43 (Y)	-2.75 (Ir)	-4.32	2.00 (Y)	-0.44 (Ir)
AuSc	-5.74	3.86 (Sc)	-4.08 (Au)	-4.75	1.96 (Sc)	-2.10 (Au)
Ni ₅ Sc	-4.31	3.86 (Sc)	-3.63 (Ni)	-3.99	1.96 (Sc)	-1.70 (Ni)
AuLu	-5.82	3.84 (Lu)	-4.25 (Au)	-4.64	1.60 (Lu)	-1.88 (Au)
Au ₃ Lu	-4.72	3.84 (Lu)	-4.08 (Au)	-4.13	1.60 (Lu)	-1.71 (Au)
Co ₃ Y	-5.22	3.67 (Y)	-3.40 (Co)	-4.61	-0.37 (Y)	0.44 (Co)
PtZr	-5.82	3.58 (Zr)	-3.58 (Pt)	-4.80	1.74 (Zr)	-1.61 (Pt)
Ni ₃ Zr	-4.43	3.58 (Zr)	-2.85 (Ni)	-4.04	1.74 (Zr)	-1.29 (Ni)
IrW	-5.36	3.24 (W)	-1.76 (Ir)	-4.83	2.02 (W)	-0.87 (Ir)
AgHf ₂	-5.99	3.22 (Hf)	-3.44 (Ag)	-4.79	1.41 (Hf)	-1.63 (Ag)
Au ₃ Hf	-4.96	3.22 (Hf)	-5.06 (Au)	-4.37	1.41 (Hf)	-2.70 (Au)
Ni ₄ W	-4.44	3.16 (W)	-3.33 (Ni)	-4.27	1.95 (W)	-2.50 (Ni)
IrNb	-5.26	3.08 (Nb)	-1.57 (Ir)	-4.63	1.59 (Nb)	-0.47 (Ir)
Cd ₃ Nb	-4.69	3.08 (Nb)	-3.94 (Cd)	-4.36	1.59 (Nb)	-2.63 (Cd)
Ir ₃ Y	-5.79	3.03 (Y)	-2.55 (Ir)	-5.08	0.74 (Y)	-0.32 (Ir)
PdTa	-5.47	3.02 (Ta)	-3.43 (Pd)	-4.69	1.47 (Ta)	-1.88 (Pd)
Pd ₃ Ta	-4.59	3.02 (Ta)	-3.44 (Pd)	-4.33	1.47 (Ta)	-2.42 (Pd)
Pt ₃ Ta	-4.81	3.02 (Ta)	-3.76 (Pt)	-4.28	1.47 (Ta)	-1.71 (Pt)
Rh ₂ Ta	-4.89	3.02 (Ta)	-2.39 (Rh)	-4.52	1.47 (Ta)	-1.41 (Rh)
AuMn	-5.19	2.99 (Mn)	-2.97 (Au)	-5.00	2.59 (Mn)	-2.59 (Au)
Ir ₂ Lu	-5.55	2.95 (Lu)	-2.23 (Ir)	-4.74	0.80 (Lu)	-0.12 (Ir)
Cu ₃ Ti ₂	-5.04	2.89 (Ti)	-3.34 (Cu)	-4.54	1.46 (Ti)	-2.10 (Cu)

From the table we find, as somehow expected, that compounds formed from elements placed at the different edges of the d -metal period present the largest ΔE_{el} . In general one finds that the binding energy of the most reactive elements, typically Y, Sc, Lu, Zr, Hf, W, Nb and Ta, is drastically reduced (up to 4 eV) with respect to that of the corresponding elemental phase. At the same time, E_{b}^{O} of the least reactive element increases, often by a relatively similar amount. Such variations are significantly more pronounced when considering binding to O than to S, mostly because the binding energies to O are larger and because their dependence on the d -band filling factor is more pronounced (see Fig. 1). Interestingly, we can identify compounds whose composition-averaged binding energy is relatively low, $\tilde{E}_{\text{b}} > -4.5$ eV for O, and similar for O and S (within some fraction of eV), and at the same time present inequivalent sites that bind drastically differently from their elemental phases. These are mostly Ni-based intermetallics such as Ni₅Sc ($\tilde{E}_{\text{b}}^{\text{O}} = -4.31$ eV, $\tilde{E}_{\text{b}}^{\text{S}} - \tilde{E}_{\text{b}}^{\text{O}} = 0.32$ eV), Ni₄W (-4.44 eV, 0.17 eV), Ni₃Zr (-4.43 eV, 0.39 eV), and also Pd₃Ta (-4.59 eV,

0.36 eV) and Cu₅Y (-4.38 eV, 0.39 eV).

E. Ternary alloys

Finally we turn our attention to the ternary compounds. In this case the set available is significantly smaller than what found for the binaries, and in fact the same search criterion used before now returns us only 50 ternary phases. This may look a bit surprising, since ICSD approximately counts about 40,000 binary and 75,000 ternary phases⁶. However, here we are considering only compounds made of transition metals. These are then prone to form solid state solutions or highly disordered phases²⁵, whose structures are typically not part of ICSD. Furthermore, we have only included the compounds that are both in ICSD and AFLOWLIB.org library⁵, namely at the intersection of the ‘real (ICSD)’ (the subset of ICSD reporting experimentally determined structures) and the ‘*ab initio* (AFLOWlib)’ database. In any case, the ternaries considered can be found from the union of the sets $S_{3d} = [\text{Sc-Zn}]$, $S_{4d} = [\text{Y-Zr, Mo, Ru, Pd-Cd}]$ and $S_{5d} = [\text{Lu-Hf, W-Re, Pt-Hg}]$, namely they may contain any of the $3d$ element and a selection of the $4d$ and $5d$, with a preference for either early or late transition metals.

In Fig. 8 we show the list of these ternary compounds sorted by their composition-averaged binding energy, while details of the site-dependent binding energy together with the associated elemental energy shifts are provided in Table IV in the appendix. In general, as expected, the ternary phases showing shallower \tilde{E}_{b} are those including late transition metals, often going beyond the noble ones (e.g. Zn and Cd). More interestingly, the subset for which \tilde{E}_{b} is approximately the same for O and S are those with an average electronic configuration close to s^2d^9 , namely that of Cu, Ag and Au. These, for instance include, Cu₂NiZn, CdPt₂Zn, AuCuZn₂ and AuCuCd₂. Among them, Cu₂NiZn appears particularly interesting, since it mimics the electronic structure of a noble metal, without including expensive elements. In contrast, at the opposite side of the distribution we find alloys with a dominant early transition-metal composition, for which the binding energy is deep and asymmetric between O and S.

F. Model validation for binary and ternary alloys

In closing this results section we are finally coming back to the question of the accuracy of our model and the limits of its predictions. We have already remarked (see section III A) that the spread in the DFT binding energies across different surfaces for elemental $4d$ transition-metal compounds is in the region of 2 eV (± 1 eV). Here we aim at validating such error for binary and ternary alloys.

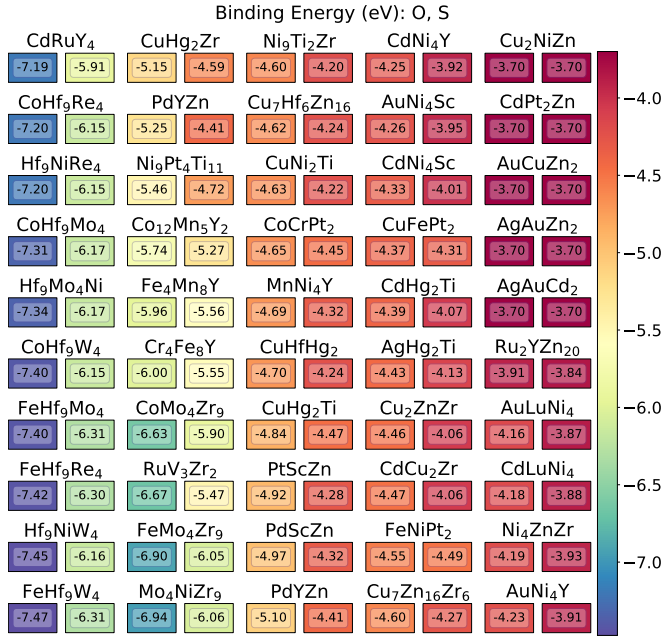


FIG. 8. (Colour online): Composition-averaged binding energy for all the ternary compounds investigated. The two rectangles below each compound refer to O (left-hand side) and S (right-hand side), respectively, and include the composition-averaged binding energy. The boxes are then colour coded with the same quantity for an easy visualization.

To this goal we have selected four binary compounds and one ternary and computed the DFT binding energies for O and S for several different surfaces. The compounds in questions are AgZr (ICSD number 605996), AgZr₃ (58392), CuPd (181913), Cu₃Pd (103084) and CuHfHg₂ (102969). In particular we have selected two phases from the Ag-Zr binary system, as elemental Ag and Zr provide strongly and weakly coupling binding sites, respectively; and two compounds from the Cu-Pd system, since it is a low binding-energy one, and hence interesting for applications. Finally, we have considered CuHfHg₂, since it includes elements with a broad range of binding strengths to O and S. For those we have computed the binding energies at the (100), (110) and (111) surfaces, and whenever inequivalent, at the (001) one. Note that some of these compounds present a layered structure, so that different surface terminations are possible. In this case we have computed the binding energy for all the inequivalent terminations. The calculations then proceed as for the elemental phases, by finding the minimum energy binding site, and its corresponding, E_b .

Our results are summarised in Fig. 9, where we report all the computed binding energies and we colour-code the specific binding sites (the dominant site in the case the adsorbant coordinates with atoms belonging to different species). Let us start from the Ag-Zr system. In general this presents a bimodal distribution, with Zr-dominated binding sites showing low binding energies

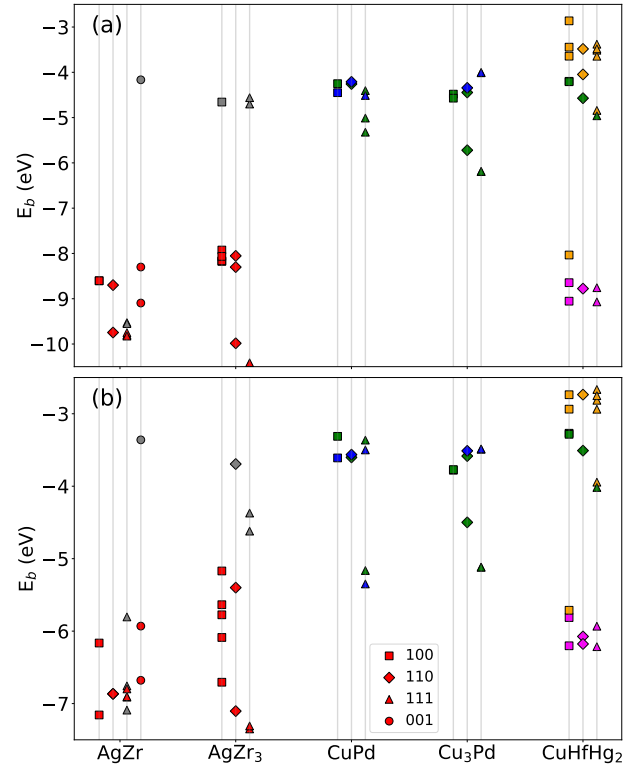


FIG. 9. (Colour online): DFT-computed binding energies of O (a) and S (b) for a number of selected binary and ternary compounds: AgZr (ICSD #605996) and AgZr₃ (ICSD #58392); CuPd (ICSD #181913), Cu₃Pd (ICSD #103084) and CuHfHg₂ (ICSD #102969). For each compound we report the binding energy of different surfaces and different absorption sites. Note that for the same surface orientation there may be different possible terminations. Different symbols correspond to different surfaces (the colour is that of the dominant binding specie). The colour code is as following: Ag = grey, Cu = green, Hf = magenta, Hg = orange, Pd = blue, Zr = red.

and Ag-dominated ones binding in a much weaker way. In particular, the Zr sites have binding energies ranging from -10 eV to -8 eV for O and from -7 eV to -5 eV for S, while the Ag ones are around -4.5 eV for O and -3.5 eV for S. These values have to be compared with those predicted by our model by using the bulk DOS (see Fig. 6). For the Zr-Ag system the model returns a binding energy range of [-7, -5] eV for O and [-6.5, -4.5] eV for S. Thus, we find that our model is capable of predicting the low binding-energy side of our distribution relatively well, while it appears to miss some Zr binding sites with extremely low binding energy (it predicts the upper side of the Zr distribution). These are associated with electron-depleted Zr-dominated surfaces, namely having electronic structure rather different from that of the bulk.

The situation is significantly better for the Cu-Pd system, where DFT returns a binding energy range of [-6,-

4] eV for O and [-5,-3.5]eV for S, to be compared with a rather uniform model prediction of -4 eV for both O and S. Such result is not surprising, since the electronic structure of Pd and Cu are rather similar, so that large fluctuations at surfaces are not expected. Finally, when looking at our ternary compound we find a tri-modal distribution of binding energies with those associated to Hf at -9 eV (-6 eV), those to Cu at -4.5 eV (-3.5 eV) and those to Hg at -3.5 eV (-3 eV) for O (S). For ternary alloys our model was used only to predict the composition-averaged binding energy, which is -4.7 eV for O and -4.24 eV for S. The composition-averaged E_b computed from the DFT values are -5.13 eV for O and -3.88 eV for S, namely in quite good agreement with the model.

IV. CONCLUSION AND OUTLOOK

We have here investigated the propensity to oxidation and tarnishing of a large set of binary and ternary inter-metallic compounds. These were selected among existing phases, as reported in the ICSD and AFLOWLIB.org databases. Such large-scale screening was enabled by taking the binding energy to O and S as a proxy to the first stage of the corrosion process and by the definition of a descriptor. More specifically, we have utilised the well-known d -band-position concept and constructed a descriptor with the associated parameters being fitted to DFT calculations for the $4d$ transition metal series. A number of variants of the original Newns-Anderson model were evaluated before choosing one based on an analytical semi-elliptical density of states. Such descriptor was then put to work against the electronic structures contained in AFLOWLIB.org, after appropriate fitting, to investigate trends in the binding energy across the compositional space.

In general, we have found the binding to O to be significantly stronger than that to S, a fact that follows closely the behaviour of the enthalpy of formation of oxides and sulphides. Such difference, however, gets reduced as one moves across the transition metal period towards the s^2d^9 atomic configuration (s^1d^{10} in the solid state), characteristic of Cu, Ag and Au. A somewhat similar situation is found for binary and ternary compounds. In this case, however, the presence of chemically and structurally inequivalent sites complicate the analysis, which is better performed by computing for each compound and binary system the largest and smallest binding energies. This reveals binary systems presenting the co-existence of strongly and weakly binding sites, composed of an early and a late transition metal. At the same time, binary phases made of elements belonging to adjacent groups display little variation in binding energy with the particular binding site.

The thermodynamical information contained in the binding energy can be then converted into a proxy for the reactivity by using the so-called Brønsted-Evans-Polanyi relations. These are directly available for O_2 and have

been extrapolated also to S_2 . By using such relations we have established that, at ambient conditions (temperature and relative S/O abundance), early-stage corrosion to O and S compete only when the binding energies are comparable, otherwise oxidation always appears to dominate. This first situation takes place only for late, and usually expensive, transition-metal alloys. However, in the ternary space this seems to be possible also for a handful of alloys presenting an average s^1d^{10} configuration, but not necessarily including Ag and Au, such as Cu_2NiZn .

Overall our work provides a first rough navigation map across the binary and ternary transition metal composition space, which is useful to categorise materials according to their propensity to oxidation and tarnishing. Certainly, our method has several limitations, which need to be overcome in order to establish a high-throughput quantitative theory of surface reactivity across such vast chemical and structural space. Firstly, we need to improve over our binding-energy prediction ability. For instance, our descriptor is completely agnostic to the specific surface and absorption site. One first improvement may be that of running the NA model over the specific surface DOS, an operation that, however, will require DFT surface calculations for the entire database, a numerically daunting task. In that case one may include additional features of the surface DOS into the model, which is likely to become more accurate.²⁰ An alternative strategy is to develop models taking into account the possibly bonding geometry of the different bonding sites. If machine-learning schemes²⁶ can be constructed, this may limit the number of surface calculations to perform.

Secondly, we need to establish a more solid link between the binding energy and the surface chemical activity. In this case, one has to validate a new set of Brønsted-Evans-Polanyi relations for O- and S-containing atmospheric gases,²⁷ such as H_2S or SO_2 . This will involve performing reaction path calculations over a range of surfaces. The task is relatively straightforward for elemental phases, but becomes much more complex in the case of binary and ternary alloys. Also in this case a machine-learning strategy generalising or replacing completely the Brønsted-Evans-Polanyi approach may be a possible solution. A few examples in such direction exist^{28,29}, but to date the field remains quite uncharted.

ACKNOWLEDGEMENT

We thank Corey Oses, Cormac Toher and Stefano Curtarolo for support with the AFLOWLIB.org API. This work is supported by Science Foundation Ireland (Amber center 12/RC/2278) and by Nokia Bell Lab. Computational resources have been provided by the super-computer facilities at the Trinity Center for High Performance Computing (TCHPC) and at the Irish Center for High End Computing (ICHEC), projects (tcphy108c and

tcphy120c).

Appendix A: Semi-circular density of state

We consider the Anderson impurity model for the adsorbate problem, defined as follows. We consider the impurity with onsite level, ϵ_a , coupled to the s - p and the d band of a transition metal. The band dispersions for the metal are $\epsilon_{\mathbf{k}}^s$ and $\epsilon_{\mathbf{k}}^d$. One can then write the following Hamiltonian [see Eq.(3)],

$$H = \underbrace{\sum_{\sigma} \epsilon_a a_{\sigma}^{\dagger} a_{\sigma}}_{\text{Impurity}} + \underbrace{\sum_{\mathbf{k}\sigma} \epsilon_{\mathbf{k}}^s s_{\mathbf{k}\sigma}^{\dagger} s_{\mathbf{k}\sigma} + \epsilon_{\mathbf{k}}^d d_{\mathbf{k}\sigma}^{\dagger} d_{\mathbf{k}\sigma}}_{s-d \text{ band dispersion}} + \underbrace{\sum_{\mathbf{k}\sigma} V_{\mathbf{k}}^s a_{\sigma}^{\dagger} s_{\mathbf{k}\sigma} + V_{\mathbf{k}}^d a_{\sigma}^{\dagger} d_{\mathbf{k}\sigma} + \text{h.c.}}_{\text{Impurity-band coupling}}, \quad (\text{A1})$$

where $V_{\mathbf{k}}^s$ and $V_{\mathbf{k}}^d$ are the coupling integrals of the s - p and d band to the impurity level. The operator a_{σ}^{\dagger} (a_{σ}) creates (annihilates) an electron in the impurity level, while the $s_{\mathbf{k}\sigma}^{\dagger}$ ($s_{\mathbf{k}\sigma}$) and $d_{\mathbf{k}\sigma}^{\dagger}$ ($d_{\mathbf{k}\sigma}$) do the same for an electron in the bulk state $|\mathbf{k}\sigma\rangle_{s,d}$ of the s - p and d bands respectively. Since there is no mixing in the spins, for the moment we drop the spins label σ .

Now let's calculate the impurity density of state (DOS). We define the impurity and mixed Green's functions as follows,

$$G_{aa}(t) = -i\theta(t)\langle [a(t), a^{\dagger}(0)] \rangle, \quad (\text{A2})$$

$$G_{ad}(\mathbf{k}, t) = -i\theta(t)\langle [d_{\mathbf{k}}(t), a^{\dagger}(0)] \rangle, \quad (\text{A3})$$

$$G_{as}(\mathbf{k}, t) = -i\theta(t)\langle [s_{\mathbf{k}}(t), a^{\dagger}(0)] \rangle, \quad (\text{A4})$$

where, $d_{\mathbf{k}}(t) = e^{iHt}d_{\mathbf{k}}e^{-iHt}$ and so on. The equation of motion for these Green's function are

$$i\frac{\partial G_{aa}(t)}{\partial t} = \delta(t) + i\theta(t)\langle [[H, a(t)], a^{\dagger}(0)] \rangle, \quad (\text{A5})$$

$$i\frac{\partial G_{ad}(\mathbf{k}, t)}{\partial t} = i\theta(t)\langle [[H, d_{\mathbf{k}}(t)], a^{\dagger}(0)] \rangle, \quad (\text{A6})$$

$$i\frac{\partial G_{as}(\mathbf{k}, t)}{\partial t} = i\theta(t)\langle [[H, s_{\mathbf{k}}(t)], a^{\dagger}(0)] \rangle. \quad (\text{A7})$$

It is easy to see, that $[H, a] = -\epsilon_a a - \sum_{\mathbf{k}} V_{\mathbf{k}}^s s_{\mathbf{k}} - \sum_{\mathbf{k}} V_{\mathbf{k}}^d d_{\mathbf{k}}$, $[H, s_{\mathbf{k}}] = -\epsilon_{\mathbf{k}}^s s_{\mathbf{k}} - V_{\mathbf{k}}^{s*} a$, and $[H, d_{\mathbf{k}}] = -\epsilon_{\mathbf{k}}^d d_{\mathbf{k}} - V_{\mathbf{k}}^{d*} a$, where $V_{\mathbf{k}}^{s*}$ is complex conjugate of $V_{\mathbf{k}}^s$. By using these identities, the equations of motion simplify to,

$$i\frac{\partial G_{aa}(t)}{\partial t} = \delta(t) + \epsilon_a G_{aa}(t) + \sum_{\mathbf{k}} (V_{\mathbf{k}}^d G_{ad}(\mathbf{k}, t) + V_{\mathbf{k}}^s G_{as}(\mathbf{k}, t)), \quad (\text{A8})$$

$$i\frac{\partial G_{ad}(\mathbf{k}, t)}{\partial t} = \epsilon_{\mathbf{k}}^d G_{ad}(\mathbf{k}, t) + V_{\mathbf{k}}^{d*} G_{aa}(t), \quad (\text{A9})$$

$$i\frac{\partial G_{as}(\mathbf{k}, t)}{\partial t} = \epsilon_{\mathbf{k}}^s G_{as}(\mathbf{k}, t) + V_{\mathbf{k}}^{s*} G_{aa}(t), \quad (\text{A10})$$

which in Fourier space become algebraic equations,

$$(\omega - \epsilon_a)G_{aa}(\omega) = 1 + \sum_{\mathbf{k}} (V_{\mathbf{k}}^d G_{ad}(\mathbf{k}, \omega) + V_{\mathbf{k}}^s G_{as}(\mathbf{k}, \omega)), \quad (\text{A11})$$

$$(\omega - \epsilon_{\mathbf{k}}^d)G_{ad}(\mathbf{k}, \omega) = V_{\mathbf{k}}^{d*} G_{aa}(\omega), \quad (\text{A12})$$

$$(\omega - \epsilon_{\mathbf{k}}^s)G_{as}(\mathbf{k}, \omega) = V_{\mathbf{k}}^{s*} G_{aa}(\omega). \quad (\text{A13})$$

Now, by substituting $G_{as}(\mathbf{k}, \omega)$ and $G_{ad}(\mathbf{k}, \omega)$ from Eq. (A12) into Eq. (A11) we obtain the impurity Green's function

$$(\omega - \epsilon_a)G_{aa}(\omega) = 1 + \sum_{\mathbf{k}} \left(\frac{|V_{\mathbf{k}}^d|^2}{\omega - \epsilon_{\mathbf{k}}^d + i\eta} + \frac{|V_{\mathbf{k}}^s|^2}{\omega - \epsilon_{\mathbf{k}}^s + i\eta} \right) G_{aa}(\omega), \quad (\text{A14})$$

or, simplifying

$$G_{aa}(\omega) = \frac{1}{\omega - \epsilon_a - \sum_{\mathbf{k}} \left(\frac{|V_{\mathbf{k}}^d|^2}{\omega - \epsilon_{\mathbf{k}}^d + i\eta} + \frac{|V_{\mathbf{k}}^s|^2}{\omega - \epsilon_{\mathbf{k}}^s + i\eta} \right)} \quad (\text{A15})$$

$$= \frac{1}{\omega - \epsilon_a - \Sigma(\omega)}, \quad (\text{A16})$$

where $\Sigma(\omega)$ is the self energy given by

$$\Sigma(\omega) = \sum_{\mathbf{k}} \left(\frac{|V_{\mathbf{k}}^d|^2}{\omega - \epsilon_{\mathbf{k}}^d + i\eta} + \frac{|V_{\mathbf{k}}^s|^2}{\omega - \epsilon_{\mathbf{k}}^s + i\eta} \right). \quad (\text{A17})$$

Now consider the imaginary part of the self energy ($\lim \eta \rightarrow 0$), which is readily related to the DOS,

$$\begin{aligned} \text{Im}\Sigma(\omega) &= - \sum_{\mathbf{k}} \left(\frac{|V_{\mathbf{k}}^d|^2 \eta}{(\omega - \epsilon_{\mathbf{k}}^d)^2 + \eta^2} + \frac{|V_{\mathbf{k}}^s|^2 \eta}{(\omega - \epsilon_{\mathbf{k}}^s)^2 + \eta^2} \right) \\ &= \pi \sum_{\mathbf{k}} (|V_{\mathbf{k}}^d|^2 \delta(\omega - \epsilon_{\mathbf{k}}^d) + |V_{\mathbf{k}}^s|^2 \delta(\omega - \epsilon_{\mathbf{k}}^s)). \end{aligned} \quad (\text{A18})$$

If we assume the couplings to be independent of \mathbf{k} , namely $V_{\mathbf{k}}^d = V_d$ and $V_{\mathbf{k}}^s = V_s$, we have the following

$$\begin{aligned} \text{Im}\Sigma(\omega) &= \pi V_d^2 \sum_{\mathbf{k}} \delta(\omega - \epsilon_{\mathbf{k}}^d) + \pi V_s^2 \sum_{\mathbf{k}} \delta(\omega - \epsilon_{\mathbf{k}}^s) \\ &= \pi V_d^2 D_d(\omega) + \pi V_s^2 D_s(\omega) = \pi \Delta(\omega), \end{aligned} \quad (\text{A19})$$

where $D_s(\omega)$ and $D_d(\omega)$, are the density of states of the s - p and d bands. Thus, $\text{Im}\Sigma(\omega) = \pi \Delta(\omega)$, and using this, we have the real part of the self energy (say, $\Lambda(\omega)$) as

$$\begin{aligned} \text{Re}\Sigma(\omega) &= \Lambda(\omega) = P \int_{-\infty}^{\infty} \frac{\Delta(\omega') d\omega'}{\omega - \omega'} \\ &= V_d^2 P \int_{-\infty}^{\infty} \frac{D_d(\omega') d\omega'}{\omega - \omega'} + V_s^2 P \int_{-\infty}^{\infty} \frac{D_s(\omega') d\omega'}{\omega - \omega'}, \end{aligned} \quad (\text{A20})$$

where P denotes the principle part of the integral. Let us denote

$$\Lambda_d(\omega) = P \int_{-\infty}^{\infty} \frac{D_d(\omega') d\omega'}{\omega - \omega'}; \Lambda_s(\omega) = P \int_{-\infty}^{\infty} \frac{D_s(\omega') d\omega'}{\omega - \omega'}, \quad (\text{A21})$$

so that we have $\Lambda(\omega) = V_d^2 \Lambda_d(\omega) + V_s^2 \Lambda_s(\omega)$. Thus we have obtained the total self energy as a function of the s - p and d bands DOS

$$\Sigma(\omega) = \Lambda(\omega) - i\pi\Delta(\omega). \quad (\text{A22})$$

The impurity Green's function can then be simplified to

$$G_{aa}(\omega) = \frac{1}{\omega - \epsilon_a - \Lambda(\omega) + i\pi\Delta(\omega)}. \quad (\text{A23})$$

Finally the impurity density of state, $D_a(\omega) = -\frac{1}{\pi} \text{Im} G_{aa}(\omega)$, is given by

$$D_a(\omega) = \frac{\Delta(\omega)}{(\omega - \epsilon_a - \Lambda(\omega))^2 + \pi^2 \Delta(\omega)^2}. \quad (\text{A24})$$

If we choose a semi-circular DOS model, with center at ϵ_d and half bandwidth w_d for the d band, and center at 0 and half bandwidth w_s for s band, the two DOSs will write

$$D_d(\omega) = \frac{2}{\pi w_d} \sqrt{1 - \frac{(\omega - \epsilon_d)^2}{w_d^2}}, \quad (\text{A25})$$

$$D_s(\omega) = \frac{2}{\pi w_s} \sqrt{1 - \frac{\omega^2}{w_s^2}}. \quad (\text{A26})$$

Then an exact expression for $\Lambda_d(\omega)$ and $\Lambda_s(\omega)$ can be evaluated to

$$\Lambda_d(\omega + \epsilon_d) = \begin{cases} \frac{2}{w_d^2} (\omega + \sqrt{\omega^2 - w_d^2}) & \omega < -w_d \\ \frac{2}{w_d^2} \omega & |\omega| \leq w_d \\ \frac{2}{w_d^2} (\omega - \sqrt{\omega^2 - w_d^2}) & \omega > w_d \end{cases} \quad (\text{A27})$$

$$\Lambda_s(\omega) = \begin{cases} \frac{2}{w_s^2} (\omega + \sqrt{\omega^2 - w_s^2}) & \omega < -w_s \\ \frac{2}{w_s^2} \omega & |\omega| \leq w_s \\ \frac{2}{w_s^2} (\omega - \sqrt{\omega^2 - w_s^2}) & \omega > w_s \end{cases} \quad (\text{A28})$$

Finally, the binding energy of the impurity is defined as

$$E = \int_{-\infty}^{\omega=0} D_a(\omega) d\omega - \epsilon_a, \quad (\text{A29})$$

and it can be calculated in straight forward manner, in terms of the semi-circular DOS.

Appendix B: DFT binding energies for 4d metals

In Fig. 10 we re-plot the distribution of DFT binding energy across the 4d transition-metal space as a function of the atomic number. In particular, for each element of the 4d transition-metal series, the figure reports the average binding energy and its variance, when these are taken over the different surface orientations of both the actual structures and the hypothetical *fcc* ones.

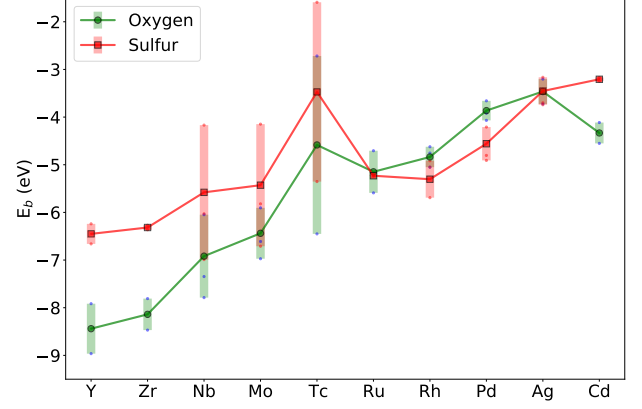


FIG. 10. (Color on line) Calculated binding energy for O and S over the 4d transition-metal series. The dots represent the average binding energy and the bar the range of values found.

Appendix C: Binding energies for ternary compounds

Appendix D: Tables with thermodynamical parameters for oxides and sulphides

TABLE IV. Composition-averaged binding energy, \tilde{E}_b , and elemental energy shift, ΔE_{el}^n ($n = A, B, C$), for all elements in the ternary compounds $A_x B_y C_z$ investigated. All energies are in eV.

$A_x B_y C_z$	Oxygen				Sulfur			
	\tilde{E}_b	ΔE_b^A	ΔE_b^B	ΔE_b^C	\tilde{E}_b	ΔE_b^A	ΔE_b^B	ΔE_b^C
Ru ₂ YZn ₂₀	-3.91	2.29	-0.45	-0.00	-3.84	1.99	-1.12	-0.00
FeMo ₄ Zr ₉	-6.90	1.60	0.72	-0.21	-6.05	1.42	0.29	-0.94
PtScZn	-4.92	0.66	0.21	0.00	-4.28	0.60	0.23	0.00
Mo ₄ NiZr ₉	-6.94	0.66	0.06	-0.28	-6.06	0.25	0.05	-0.97
CoMo ₄ Zr ₉	-6.63	0.35	0.77	0.08	-5.90	0.33	0.33	-0.80
CoHf ₉ Re ₄	-7.20	0.35	-0.89	0.20	-6.15	0.33	-1.33	-0.01
CoHf ₉ Mo ₄	-7.31	0.35	-0.97	0.01	-6.17	0.33	-1.34	-0.10
CoHf ₉ W ₄	-7.40	0.35	-1.04	-0.14	-6.15	0.33	-1.30	-0.49
Fe ₄ Mn ₈ Y	-5.96	0.24	0.72	1.40	-5.56	0.23	0.62	0.83
PdYZn	-5.10	0.11	0.26	0.00	-4.41	0.10	-0.13	0.00
PdScZn	-4.97	0.11	0.06	0.00	-4.32	0.10	0.11	0.00
PdYZn	-5.25	0.11	-0.22	0.00	-4.41	0.10	-0.13	0.00
MnNi ₄ Y	-4.69	0.06	0.06	1.43	-4.32	0.06	0.05	0.83
Ni ₉ Pt ₄ Ti ₁₁	-5.46	0.06	0.66	-0.92	-4.72	0.05	0.60	-0.72
Ni ₄ ZnZr	-4.19	0.06	0.00	0.61	-3.93	0.05	0.00	0.37
Ni ₉ Ti ₂ Zr	-4.60	0.06	-1.01	0.54	-4.20	0.05	-0.81	0.27
CdRuY ₄	-7.19	0.00	2.29	-0.72	-5.91	0.00	1.99	-1.28
AuLuNi ₄	-4.16	0.00	1.07	0.06	-3.87	0.00	0.56	0.05
CdLuNi ₄	-4.18	0.00	0.99	0.06	-3.88	0.00	0.51	0.05
CdPt ₂ Zn	-3.70	0.00	0.66	0.00	-3.70	0.00	0.60	0.00
AuNi ₄ Y	-4.23	0.00	0.06	1.27	-3.91	0.00	0.05	0.77
CdNi ₄ Y	-4.25	0.00	0.06	1.13	-3.92	0.00	0.05	0.67
AuNi ₄ Sc	-4.26	0.00	0.06	0.50	-3.95	0.00	0.05	0.46
CdNi ₄ Sc	-4.33	0.00	0.06	0.06	-4.01	0.00	0.05	0.11
Cu ₂ NiZn	-3.70	0.00	0.06	0.00	-3.70	0.00	0.05	0.00
CuNi ₂ Ti	-4.63	0.00	0.06	-0.83	-4.22	0.00	0.05	-0.63
Cu ₂ ZnZr	-4.46	0.00	0.00	0.55	-4.06	0.00	0.00	0.32
CdCu ₂ Zr	-4.47	0.00	0.00	0.49	-4.06	0.00	0.00	0.29
CdHg ₂ Ti	-4.39	0.00	0.00	0.13	-4.07	0.00	0.00	-0.01
AgAuCd ₂	-3.70	0.00	0.00	0.00	-3.70	0.00	0.00	0.00
AgAuZn ₂	-3.70	0.00	0.00	0.00	-3.70	0.00	0.00	0.00
AuCuZn ₂	-3.70	0.00	0.00	0.00	-3.70	0.00	0.00	0.00
AgHg ₂ Ti	-4.43	0.00	0.00	-0.03	-4.13	0.00	0.00	-0.26
Cu ₇ Zn ₁₆ Zr ₆	-4.60	0.00	0.00	-0.77	-4.27	0.00	0.00	-1.02
CuHg ₂ Ti	-4.84	0.00	0.00	-1.67	-4.47	0.00	0.00	-1.61
CuHg ₂ Zr	-5.15	0.00	0.00	-2.22	-4.59	0.00	0.00	-1.80
CuFePt ₂	-4.37	0.00	-0.38	0.66	-4.31	0.00	-0.41	0.60
CuHfHg ₂	-4.70	0.00	-0.78	0.00	-4.24	0.00	-0.74	0.00
Cu ₇ Hf ₆ Zn ₁₆	-4.62	0.00	-1.25	0.00	-4.24	0.00	-1.21	0.00
FeHf ₉ Re ₄	-7.42	-0.07	-0.94	0.15	-6.30	0.02	-1.33	-0.03
FeHf ₉ Mo ₄	-7.40	-0.07	-0.89	0.03	-6.31	0.02	-1.35	-0.10
FeHf ₉ W ₄	-7.47	-0.11	-0.93	-0.11	-6.31	-0.01	-1.31	-0.50
RuV ₃ Zr ₂	-6.67	-0.24	0.02	-0.00	-5.47	-0.16	0.03	0.03
FeNiPt ₂	-4.55	-0.34	-0.74	0.66	-4.49	-0.38	-0.69	0.60
Cr ₄ Fe ₈ Y	-6.00	-0.37	0.31	1.11	-5.55	-0.59	0.30	0.74
CoCrPt ₂	-4.65	-0.76	-0.38	0.66	-4.45	-0.65	-0.38	0.60
Hf ₉ NiRe ₄	-7.20	-0.88	0.06	0.16	-6.15	-1.31	0.05	-0.03
Co ₁₂ Mn ₅ Y ₂	-5.74	-0.97	0.20	0.04	-5.27	-0.86	0.26	0.04
Hf ₉ Mo ₄ Ni	-7.34	-1.02	0.02	0.06	-6.17	-1.36	-0.10	0.05
Hf ₉ NiW ₄	-7.45	-1.09	0.06	-0.13	-6.16	-1.30	0.05	-0.49

TABLE V. Summary table of structural information and enthalpy of formation, ΔH_f , for 3d transition-metal oxides. Note that there are compounds for which the information is incomplete. Data from this table has been included in Fig. 1.

Z	Compound	SG	Lattice Constants (Å)	ΔH_f (kcal mol ⁻¹)	ΔH_f /atom (eV)	Ref.
21 Sc	Sc ₂ O ₃	$Ia\bar{3}$	9.79, 9.79, 9.79	456	3.96	[30,31]
22 Ti	Ti ₆ O	$P\bar{3}1c$	5.13, 5.13, 9.48			[32]
	Ti ₃ O	$P\bar{3}1c$	5.15, 5.15, 9.56			[32]
	Ti ₂ O	$P\bar{3}m1$	2.9194, 2.9194, 4.713			[33]
	Ti ₃ O ₂	$P6/mmm$				[34]
	TiO	$P\bar{6}m2$	3.031, 3.031, 3.2377	129.5	2.81	[35,31]
	Ti ₂ O ₃	$R\bar{3}c$	5.126, 5.126, 13.878	363.29	3.15	[36,31]
	Ti ₃ O ₅	$C2/m$	9.752, 3.802, 9.442	587.72	3.19	[37,31]
	TiO ₂	$P4_2/mnm$	4.6257, 4.6257, 2.9806	225.6	3.26	[38,31]
	TiO ₂	$I4_1/amd$	3.771, 3.771, 9.43	224.9	3.25	[39,31]
23 V	VO	$Fm\bar{3}m$	4.0678, 4.0678, 4.0678	170.60	3.7	[40,31]
	V ₅ O ₉	$P\bar{1}$	7.005, 8.3629, 10.9833			[41]
	V ₄ O ₇	$P\bar{1}$	5.504, 7.007, 10.243			[42]
	V ₃ O ₅	Cc	9.98, 5.03, 9.84			[43]
	V ₂ O ₃	$R\bar{3}c$	4.9776, 4.9776, 13.9647	291.3	2.53	[44,31]
	VO ₂	$P4_2/mnm$	4.53, 4.53, 2.869	170.6	2.47	[45,31]
	V ₆ O ₁₃	$C2/m$	11.922, 3.68, 10.138			[46]
	V ₂ O ₅	$Pmn2_1$	11.48, 4.36, 3.555	370.46	2.3	[47,31]
24 Cr	Cr ₂ O ₃	$R\bar{3}c$	4.9607, 4.9607, 13.599	271.2	2.35	[48,31]
	Cr ₃ O ₄			365.92	2.27	[34]
	CrO ₂	$P4_2/mnm$	4.421, 4.421, 2.917	142.9	2.07	[49,34]
	CrO ₃	$Ama2$	5.743, 8.557, 4.789	140.3	1.52	[50,31]
25 Mn	MnO	$Fm\bar{3}m$	4.444, 4.444, 4.444	91.99	1.99	[51,31]
	Mn ₃ O ₄	$I4_1/amd$	5.76, 5.76, 9.46	331.6	2.05	[52,31]
	Mn ₂ O ₃	$Ia\bar{3}$	9.42, 9.42, 9.42	229.00	1.99	[53,31]
	MnO ₂	$P4_2/mnm$	4.4, 4.4, 2.87	125.5	1.81	[54,55]
26 Fe	FeO	$Fm\bar{3}m$	4.303, 4.303, 4.303	196.8	1.71	[56,31]
	Fe ₂ O ₃	$R\bar{3}c$	5.43, 5.43, 5.43	196.8	1.71	[57,31]
	Fe ₃ O ₄	$Fd\bar{3}m$	8.3965, 8.3965, 8.3965	265.01	1.64	[58,31]
27 Co	CoO	$Fm\bar{3}m$	4.258, 4.258, 4.258	56.81	1.23	[59,31]
	Co ₃ O ₄	$Fd\bar{3}m$	8.0821, 8.0821, 8.0821	217.5	1.35	[60,31]
28 Ni	NiO	$Fm\bar{3}m$	4.1684, 4.1684, 4.1684	57.29	1.24	[61,31]
29 Cu	Cu ₂ O	$Pn\bar{3}m$	4.252, 4.252, 4.252	41.39	0.6	[62,31]
	CuO	$P2_1/c$	4.683, 3.4203, 5.1245	38.69	0.84	[63,31]
30 Zn	ZnO	$P6_3mc$	3.249, 3.249, 5.207	83.77	1.82	[64,31]

TABLE VI. Summary table of structural information and enthalpy of formation, ΔH_f , for 3d transition-metal sulphides. Note that there are compounds for which the information is incomplete. Data from this table has been included in Fig. 1.

Z	Compound	SG	Lattice Constants (Å)	ΔH_f (kcal mol ⁻¹)	ΔH_f /atom (eV)	Ref.
21 Sc	ScS	$Fm\bar{3}m$	5.166, 5.166, 5.166	57.36	1.24	[65,66]
22 Ti	Ti ₆ S					[67]
	Ti ₃ S					[67]
	Ti ₈ S ₃	$C2/m$	32.69, 3.327, 19.36			[68]
	Ti ₂ S					[67]
	TiS	$P6_3/mmc$	3.299, 3.299, 6.38	64.5	1.4	[69,31]
	Ti ₄ S ₅	$P6_3/mmc$	3.439, 3.439, 28.933			[70]
	Ti ₃ S ₄	$P6_3/mmc$	3.43, 3.43, 11.4			[71]
	Ti ₂ S ₃	$P6_3/mc$	3.422, 3.422, 11.442	147.7	1.28	[72,73]
	TiS ₂	$P\bar{3}m1$	3.397, 3.397, 5.691	97.3	1.41	[74,31]
	TiS ₃	$P2_1/m$	4.9476, 3.3787, 8.7479	100.1	1.09	[75,73]
23 V	V ₃ S	$I4m2$	9.47, 9.47, 4.589			[76]
	V ₅ S ₄	$I4/m$	8.988, 8.988, 3.224			[77]
	VS	$P6_3/mmc$	3.34, 3.34, 5.785			[78]
	V ₇ S ₈	$P3_221$	6.706, 6.706, 17.412			[77]
	V ₃ S ₄	$C2/m$	12.599, 3.282, 5.867			[79]
	V ₅ S ₈	$C2/m$	11.3, 6.6, 8.1			[79]
	VS ₄	$I2/a$	6.78, 10.42, 12.11			[80]
24 Cr	CrS	$C2/c$	3.826, 5.913, 6.089	37.19	0.81	[81,31]
	Cr ₂ S ₃	$R\bar{3}$	5.937, 5.937, 16.698			[81,31]
25 Mn	MnS	$Fm\bar{3}m$	5.24, 5.24, 5.24	51.19	1.11	[82,31]
	MnS ₂	$Pa\bar{3}$	6.083, 6.083, 6.083	49.50	0.72	[83,31]
26 Fe	FeS	$P6_3/mmc$	3.445, 3.445, 5.763	24.0	0.52	[84,31]
	Fe ₃ S ₄	$Fd\bar{3}m$	9.876, 9.876, 9.876			[85,31]
	FeS ₂	$Pa\bar{3}$	5.4179, 5.4179, 5.4179	40.99	0.59	[86,31]
27 Co	Co ₉ S ₈	$Fm\bar{3}m$	9.927, 9.927, 9.927	22.61	0.49	[87,31]
	Co ₃ S ₄	$Fd\bar{3}m$	9.401, 9.401, 9.401	85.8	0.53	[88,31]
	CoS ₂	$Pa\bar{3}$	5.5385, 5.5385, 5.5385	36.59	0.53	[89,31]
28 Ni	Ni ₃ S ₂	$R32$	4.049, 4.049, 4.049	51.70	0.45	[90,31]
	NiS	$P6_3mc$	3.4456, 3.4456, 5.405	23.4	0.51	[91,31]
	Ni ₃ S ₄	$Fd\bar{3}m$	9.65, 9.65, 9.65	71.99	0.45	[92,31]
	NiS ₂	$Pa\bar{3}$	5.6873, 5.6873, 5.6873	29.85	0.43	[93,94]
29 Cu	Cu ₂ S	$Pa\bar{3}$	5.7891, 5.7891, 5.7891	19.0	0.27	[95,31]
	CuS	$P6_3/mmc$	3.7938, 3.7938, 16.341	12.5	0.27	[96,31]
30 Zn	ZnS	$P6_3mc$	3.8227, 3.8227, 6.2607	49.0	1.06	[97,31]

TABLE VII. Summary table of structural information and enthalpy of formation, ΔH_f , for 4d transition-metal oxides. Note that there are compounds for which the information is incomplete. Data from this table has been included in Fig. 1.

Z	Compound	SG	Lattice Constants (Å)	ΔH_f (kcal mol ⁻¹)	ΔH_f (eV)	Ref.
39 Y	Y ₂ O ₃	$Ia\bar{3}$	10.596, 10.596, 10.596	455.37	3.95	[98,31]
40 Zr	ZrO ₂	$P2_1/c$	5.1462, 5.2082, 5.3155	262.9	3.8	[99,31]
	ZrO ₂	$P4_2/nmc$	3.5781, 3.5781, 5.1623	262.9	3.8	[100,31]
	ZrO ₂	$Fm\bar{3}m$	5.1291, 5.1291, 5.1291	262.9	3.8	[101,31]
41 Nb	NbO	$Pm\bar{3}m$	4.2, 4.2, 4.2	100.31	2.17	[102,31]
	NbO ₂	$I4_1/a$	13.66, 13.66, 5.964	190.30	2.75	[103,34]
	Nb ₂ O ₅	$I4/mmm$	20.44, 20.44, 3.832	454.00	2.81	[104,31]
42 Mo	MoO ₂	$P2_1/c$	5.584, 4.842, 5.608	140.51	2.03	[105,31]
	MoO ₃	$Pnma$	13.825, 3.694, 3.954	178.11	1.93	[106,31]
43 Tc	TcO ₂	$P1_2/c$	5.6891, 4.7546, 5.5195	109.42	1.58	[107,108]
	Tc ₂ O ₇	$Pbca$	13.756, 7.439, 5.617	269.24	1.30	[109,108]
44 Ru	RuO ₂	$P4_2/mnm$	4.4968, 4.4968, 3.1049	72.9	1.05	[110,31]
45 Rh	Rh ₂ O ₃	$Pbca$	5.1477, 5.4425, 14.6977	84.99	0.74	[111,31]
46 Pd	PdO	$P4_2/mmc$	3.03, 3.03, 5.33	27.61	0.60	[112,31]
47 Ag	Ag ₂ O	$Pn\bar{3}m$	4.7306, 4.7306, 4.7306	7.43	0.11	[113,31]
48 Cd	CdO	$Fm\bar{3}m$	4.699, 4.699, 4.699	61.76	1.34	[114,31]

TABLE VIII. Summary table of structural information and enthalpy of formation, ΔH_f , for 4d transition-metal sulphides. Note that there are compounds for which the information is incomplete. Data from this table has been included in Fig. 1.

Z	Compound	SG	Lattice Constants (Å)	ΔH_f (kcal mol ⁻¹)	ΔH_f (eV)	Ref.
39 Y	Y ₂ S ₃	<i>P2₁/m</i>	17.5234, 4.0107, 10.1736			[115]
40 Zr	Zr ₃ S ₂	<i>P6m2</i>	3.429, 3.429, 3.428	88.34	0.77	[116]
	ZrS	<i>Fm3m</i>	5.25, 5.25, 5.25			[105,31]
	ZrS ₂	<i>P3m1</i>	3.63, 3.63, 5.85	138	1.99	[92,31]
	ZrS ₃	<i>P2₁/m</i>	5.1243, 3.6244, 8.980	148.11	1.61	[117,116]
41 Nb	NbS	<i>P6₃/mmc</i>	3.32, 3.32, 6.46			[118]
	NbS ₂	<i>P62c</i>	3.35, 3.35, 17.94			[119]
	NbS ₂	<i>P3m1</i>	3.42, 3.42, 5.938			[120]
42 Mo	Mo ₂ S ₃	<i>P2₁/m</i>	6.092, 3.208, 8.6335	97.20	0.84	[121,31]
	MoS ₂	<i>P6₃/mmc</i>	3.169, 3.169, 12.324	65.89	0.95	[122,31]
43 Tc	TcS ₂	P1	6.456, 6.357, 6.659	53.49	0.77	[123,108]
	Tc ₂ S ₇	unknown		147	0.71	[108]
44 Ru	RuS ₂	<i>Pa3</i>	5.6106, 5.6106, 5.6106	49.21	0.71	[124,31]
45 Rh	Rh ₃ S ₄	<i>C2/m</i>	10.4616, 10.7527, 6.2648	84.54	0.52	[125,31]
	Rh ₂ S ₃	<i>Pbcn</i>	8.462, 5.985, 6.138	62.81	0.54	[126,31]
	RhS ₂	<i>Pa3</i>	5.57, 5.57, 5.57			[127,31]
46 Pd	Pd ₄ S	<i>P42₁c</i>	5.1147, 5.1147, 5.5903	16.5	0.14	[128,31]
	PdS	<i>P4₂/m</i>	6.429, 6.429, 6.611	16.90	0.37	[129,31]
	PdS ₂	<i>Pbca</i>	5.46, 5.541, 7.531	18.69	0.27	[130,31]
47 Ag	Ag ₂ S	<i>P2₁/m</i>	4.229, 6.931, 7.862	7.60	0.11	[131,31]
48 Cd	CdS	<i>P6₃mc</i>	4.137, 4.137, 6.7144	35.70	0.77	[64,31]

TABLE IX. Summary table of structural information and enthalpy of formation, ΔH_f , for 5d transition-metal oxides. Note that there are compounds for which the information is incomplete. Data from this table has been included in Fig. 1.

Z	Compound	SG	Lattice Constants (Å)	ΔH_f (kcal mol ⁻¹)	ΔH_f (eV)	Ref.
57 La	La ₂ O ₃	<i>P6₃/mmc</i>	4.057, 4.057, 6.43	429	3.72	[132,31]
72 Hf	HfO ₂	<i>P2₁/c</i>	5.1156, 5.1722, 5.2948	267.09	3.86	[133,31]
73 Ta	Ta ₂ O ₅	<i>Pccm</i>	6.217, 3.677, 7.794	489.01	3.03	[134,31]
74 W	WO ₂	<i>P4₂/mnm</i>	4.86, 4.86, 2.77	140.89	2.04	[92,31]
	W ₂ O ₅			311.20	1.93	[135,55]
	WO ₃	<i>Pnma</i>	7.57, 7.341, 7.754	201.41	2.18	[136,31]
75 Re	ReO ₂	<i>Pbcn</i>	4.8094, 5.6433, 4.6007	103.39	1.49	[92,31]
	ReO ₃	<i>Pm3m</i>	3.734, 3.734, 3.734	146.01	1.58	[137,31]
	Re ₂ O ₇	<i>P2₁2₁2₁</i>	12.508, 15.196, 5.448	298.40	1.44	[138,31]
76 Os	OsO ₂	<i>P4₂/mnm</i>	4.519, 4.519, 3.196	70.41	1.02	[139,31]
	OsO ₄	<i>C2</i>	8.66, 4.52, 4.75	94.10	0.81	[140,31]
77 Ir	IrO ₂	<i>P4₂/mnm</i>	4.5051, 4.5051, 3.1586	59.61	1.29	[141,31]
78 Pt	PtO	<i>Fm3m</i>	5.15, 5.15, 5.15	17	0.37	[142,143]
	Pt ₃ O ₄	<i>Im3</i>	6.238, 6.238, 6.238	64.05	0.40	[144,145]
	PtO ₂	<i>Pnnm</i>	4.486, 4.537, 3.138	19.1	0.28	[146,143]
79 Au	Au ₂ O ₃	<i>Fdd2</i>	12.827, 10.52, 3.838	0.81	0.017	[147,31]
80 Hg	Hg ₂ O			21.50	0.31	[55]
	HgO	<i>Pnma</i>	6.6129, 5.5208, 3.5219	21.70	0.47	[148,31]

TABLE X. Summary table of structural information and enthalpy of formation, ΔH_f , for 5d transition-metal sulphides. Note that there are compounds for which the information is incomplete. Data from this table has been included in Fig. 1.

Z	Compound	SG	Lattice Constants (Å)	ΔH_f (kcal mol ⁻¹)	ΔH_f (eV)	Ref.
57 La	LaS	$Fm\bar{3}m$	5.788, 5.788, 5.788	112.8	2.45	[149,31]
	La ₂ S ₃	$Pnma$	7.66, 4.22, 15.95	282.98	2.45	[150,31]
	LaS ₂	$Pnma$	8.131, 16.34, 4.142	162	2.34	[151,55]
72 Hf	HfS ₂	$P\bar{3}m1$	3.69, 3.69, 6.61			[152]
	HfS ₃	$P2_1/m$	5.0923, 3.5952, 8.967			[117]
73 Ta	TaS ₂	$P6_3/mmc$	3.314, 3.314, 12.097	84.61	1.22	[153,31]
	TaS ₃	$P2_1/m$	9.515, 3.3412, 14.912			[154,31]
74 W	WS ₂	$P6_3/mmc$	3.1532, 3.1532, 12.323	62	0.89	[155,31]
75 Re	ReS ₂	$P\bar{1}$	6.455, 6.362, 6.401	42.71	0.93	[156,31]
	Re ₂ S ₇			107.91	0.52	[31]
76 Os	OsS ₂	$Pa\bar{3}$	5.6194, 5.6194, 5.6194	35.11	0.51	[157,31]
77 Ir	Ir ₂ S ₃			59.61	0.52	[31]
	IrS ₂	$Pnma$	19.791, 3.5673, 5.6242	31.81	0.46	[158,31]
78 Pt	PtS	$P4_2/mmc$	3.47, 3.47, 6.1	19.86	0.43	[159,31]
	PtS ₂	$P\bar{3}m$	3.5432, 3.5432, 5.0388	26.51	0.57	[160,31]
79 Au	Au ₂ S	$Pn\bar{3}m$	5.0206, 5.0206, 5.0206			[161,31]
80 Hg	HgS	$P\bar{3}_121$	4.16, 4.16, 9.54	12.74	0.28	[162,31]

- ¹ D.R. Gunasegaram, M.S. Venkatraman, and I.S. Cole, *Int. Mater. Rev.* **59**, 84 (2014).
- ² G. Saleh, C. Xu, and S. Sanvito, *Angew. Chem. Int. Ed.* **58**, 6017 (2019).
- ³ S. Curtarolo, G. L. W. Hart, M. B. Nardelli, N. Mingo, S. Sanvito, and O. Levy, *Nature Mater.* **12**, 191 (2013).
- ⁴ B. Hammer and J. K. Nørskov, *Nature* **376**, 238 (1995).
- ⁵ *Comput. Mater. Sci.* **58**, 227 (2012).
- ⁶ D. Zagorac, H. Müller, S. Ruehl, J. Zagorac, and S. Rehme, *J. Appl. Cryst.* **52**, 918 (2019).
- ⁷ B. Hammer and J. K. Nørskov, *Surf. Sci.* **343**, 211 (1995).
- ⁸ F. Besenbacher and J. K. Nørskov, *Prog. Surf. Sci.* **44**, 5 (1993).
- ⁹ B. Hammer, Y. Morikawa, and J. K. Nørskov, *Phys. Rev. Lett.* **76**, 2141 (1996).
- ¹⁰ A. Ruban, B. Hammer, P. Stoltze, H. L. Skriver, and J. K. Nørskov, *J. Mol. Catal. A* **115**, 421 (1997).
- ¹¹ D. M. Newns, *Phys. Rev.* **178**, 1123 (1969).
- ¹² P. W. Anderson, *Phys. Rev.* **124**, 41 (1961).
- ¹³ B. Hammer and J. K. Nørskov, *Adv. Catal.* **45**, 71 (2000).
- ¹⁴ O. Andersen, O. Jepsen and D. Glötzel, *Highlights of Condensed Matter Theory, LXXXIX, p. 59. Corso Soc. Italiana di Fisica*, (1985).
- ¹⁵ V. Blum, R. Gehrke, F. Hanke, P. Havu, V. Havu, X. Ren, K. Reuter, and M. Scheffler, *Comput. Phys. Commun.* **180**, 2175 (2009).
- ¹⁶ B. Hammer, L. B. Hansen, and J. K. Nørskov, *Phys. Rev. B* **59**, 7413 (1999).
- ¹⁷ G. Kresne and J. Furthmüller, *Phys. Rev. B* **54**, 11169 (1996).
- ¹⁸ R. H. Taylor, F. Rose, C. Toher, O. Levy, K. Yang, M. Buongiorno Nardelli, and S. Curtarolo, *Comput. Mater. Sci.* **93**, 178 (2014).
- ¹⁹ J. Greeley and J. K. Nørskov, *Surf. Sci.* **592**, 104 (2005).
- ²⁰ H. Xin, A. Vojvodic, J. Voss, J.K. Nørskov and F. Abild-Pedersen, *Phys. Rev. B* **89**, 115114 (2014).
- ²¹ J.N. Brønsted, *Chem. Rev.* **5**, 231 (1928).
- ²² M. Evans and N. Polanyi, *Trans. Faraday Soc.* **34**, 11 (1938).
- ²³ J.K. Nørskov, T. Bligaard, A. Logadottir, S. Bahn, L.B. Hansen, M. Bollinger, H. Bengaard, B. Hammer, Z. Sljivancanin, M. Mavrikakis, Y. Xu, S. Dahl and C.J.H. Jacobsen, *J. Catal.* **209**, 275 (2002).
- ²⁴ A. Michaelides, Z.-P. Liu, C. J. Zhang, A. Alavi, D. A. King, and P. Hu, *J. Am. Chem. Soc.* **125**, 3704 (2003).
- ²⁵ C. Toher, C. Oses, D. Hicks, and S. Curtarolo, *Npj Comput. Mater.* **5**, 69 (2019).
- ²⁶ S. Wang, H. S. Pillai, and H. Xin, *Nature Commun.* **11**, 6132 (2020).
- ²⁷ W. Aas, A. Mortier, V. Bowersox, R. Cherian, G. Faluvegi, H. Fagerli, J. Hand, Z. Klimont, C. Galy-Lacaux, C. M. B. Lehmann, C. L. Myhre, G. Myhre, D. Olivie, K. Sato, J. Quaas, P. Rao, M. Schulz, D. Shindell, R. B. Skeie, A. Stein, T. Takemura, S. Tsyro, R. Vet, and X. Xu, *Sci. Rep.* **9**, 953 (2018).
- ²⁸ S. Stocker, G. Csányi, K. Reuter and J.T. Margraf, *Nature Commun.* **11**, 5505 (2020).
- ²⁹ B. Lee, J. Yoo and K. Kang, *Chem. Sci.* **11**, 7813 (2020).
- ³⁰ W. Milligan, L. Vernon, H. Levy, and S. Peterson, *J. Phys. Chem.* **57**, 535 (1953).
- ³¹ O. Kubaschewski, C.B. Alcock and P.J. Spencer, *Materials Thermochemistry*, Pergamon Press, Oxford (UK), (1993).
- ³² L. Fykin, V. Vavilova, I. Kornilov, S. Solovév, and R. Ozerov, *Doklady Akademii Nauk SSSR* **191**, 96 (1970).
- ³³ T. Novoselova, S. Malinov, W. Sha, and A. Zhecheva, *Mater. Sci. Eng. A* **371**, 103 (2004).
- ³⁴ D.R. Lide, *CRC Handbook of Chemistry and Physics*, CRC Press (2004).
- ³⁵ S. Moehr and H. Müller-Buschbaum, *Z. Anorg. Allg. Chem.* **620**, 1175 (1994).
- ³⁶ C.E. Rice and W.R. Robinson, *Mater. Res. Bull.* **11**, 1355 (1976).
- ³⁷ S. Åsbrink and A. Magnéli, *Acta Crystallogr.* **12**, 575 (1959).
- ³⁸ M. Okrusch, R. Hock, U. Schüssler, A. Brummer, M. Baier and H. Theisinger, *Am. Mineral.* **88**, 986 (2003).
- ³⁹ Th.E. Weirich, M. Winterer, S. Seifried, H. Fuess, and H. Hahn, *Ultramicroscopy* **81**, 263 (2000).
- ⁴⁰ D. Taylor, *Trans. J. Br. Ceram. Soc.* **83**, 5 (1984).
- ⁴¹ Y. L. Page, P. Bordet, and M. Marezio, *J. Solid State Chem.* **92**, 380 (1991).
- ⁴² H. Horiuchi, M. Tokonami, K. Nagasawa, and N. Morimoto, *Acta Crystallogr. B* **28**, 1404 (1972).
- ⁴³ S. Åsbrink, S. Friberg, A. Magnéli and G. Andersson, *Acta Chem. Scand.* **13**, 603 (1959).
- ⁴⁴ W.R. Robinson, *Acta Crystallogr. B* **31**, 1153 (1975).
- ⁴⁵ S. Westman, *Acta Chem. Scand.* **15**, 217 (1961).
- ⁴⁶ P.D. Dernier, *Mater. Res. Bull.* **9**, 955 (1974).
- ⁴⁷ J.A.A. Ketelaar, *Nature* **137**, 316 (1936).
- ⁴⁸ R.E. Newnham and Y.M. de Haan, *Z. Kristallogr.* **117**, 235 (1962).
- ⁴⁹ W.H. Baur and A.A. Khan, *Acta Crystallogr. B* **27**, 2133 (1971).
- ⁵⁰ A. Byström and K.-A. Wilhelmi, *Acta Chem. Scand.* **4**, 1131 (1950).
- ⁵¹ M. Kuriyama and S. Hosoya, *J. Phys. Soc. Jpn.* **17**, 1022 (1962).
- ⁵² K. Satomi, *J. Phys. Soc. Jpn.* **16**, 258 (1961).
- ⁵³ A. Fert, *Bulletin de la Societe Francaise de Mineralogie et de Cristallographie* **85**, 267 (1962).
- ⁵⁴ A. St. John, *Phys. Rev.* **21**, 389 (1923).
- ⁵⁵ E. Washburn, *International Critical Tables of Numerical Data, Physics, Chemistry and Technology (1st Electronic Edition)*, Knovel (1930).
- ⁵⁶ R. Wyckoff and E. Crittenden, *Z. Kristallogr.* **63**, 144 (1926).
- ⁵⁷ L. Pauling and S.B. Hendricks, *J. Am. Chem. Soc.* **47**, 781 (1925).
- ⁵⁸ C. Haavik, S. Stolen, H. Fjellvag, M. Hanfland, and D. Hausermann, *Am. Mineral.* **85**, 514 (2000).
- ⁵⁹ N.C. Tombs and H. Rooksby, *Nature* **165**, 442 (1950).
- ⁶⁰ X. Liu and C.T. Prewitt, *Phys. Chem. Miner.* **17**, 168 (1990).
- ⁶¹ R.W. Cairns and E. Ott, *J. Am. Chem. Soc.* **55**, 527 (1933).
- ⁶² M. Neuburger, *Z. Phys.* **67**, 845 (1930).
- ⁶³ H. Yamada, Y. Soejima, M. Kawaminami, and X. Zheng, *Trans. Mater. Res. Soc. Jpn.* **25**, 1199 (2000).
- ⁶⁴ Y.N. Xu and W.Y. Ching, *Phys. Rev. B* **48**, 4335 (1993).

- ⁶⁵ R.P. Steiger and E.D. Cater, *High Temp. Sci.* **2**, 398 (1970).
- ⁶⁶ R.T. Tuenge, *A high temperature vaporization and thermodynamic study of the scandium-sulfur system*, Iowa State University, PhD Thesis, (1975).
- ⁶⁷ J. Murray, *Bull. Alloy Phase Diagr.* **7**, 156 (1986).
- ⁶⁸ J.P. Owens and H.F. Franzen, *Acta Crystallogr. B* **30**, 427 (1974).
- ⁶⁹ S.F. Bartram, *Dissertation Abstracts* **19**, 1216 (1958).
- ⁷⁰ G.A. Wiegiers and F. Jellinek, *J. Solid State Chem.* **1**, 519 (1970).
- ⁷¹ H. Hahn and B. Harder, *Z. Anorg. Allg. Chem.* **288**, 241 (1956).
- ⁷² Y. Jeannin, *Ann. Chim.* **7**, 57 (1962).
- ⁷³ P.A.G. O'Hare and G.K. Johnson, *J. Chem. Thermodyn.* **18**, 189 (1986).
- ⁷⁴ I. Oftedal, *Z. Phys. Chem.* **134**, 301 (1928).
- ⁷⁵ A. Lipatov, P.M. Wilson, M. Shekhirev, J.D. Teeter, R. Netusil, and A. Sinitskii, *Nanoscale* **7**, 12291 (2015).
- ⁷⁶ B. Pedersen and F. Gronvold, *Acta Crystallogr.* **12**, 1022 (1959).
- ⁷⁷ F. Gronvold, H. Haraldsen, and B. P. T. Tufte, *Rev. Chim. Minér.* **6**, 215 (1969).
- ⁷⁸ W. Biltz and A. Koecher, *Z. Anorg. Allg. Chem.* **241**, 324 (1939).
- ⁷⁹ A.B. de Vries and F. Jellinek, *Rev. Chim. Minér.* **11**, 624 (1974).
- ⁸⁰ R. Allmann, I. Baumann, A. Kutoglu, H. Rosch, and E. Hellner, *Naturwissenschaften* **51**, 263 (1964).
- ⁸¹ F. Jellinek, *Acta Crystallogr.* **10**, 620 (1957).
- ⁸² H. Ott, *Z. Kristallogr.* **63**, 222 (1926).
- ⁸³ T.K. Chattopadhyay, H.G. von Schnering, G.J. McIntyre, and R.F.D. Stansfield, *Z. Kristallogr.* **199**, 13 (1992).
- ⁸⁴ J.-M. Shen and Y.-Y. Feng, *J. Phys. Chem. C* **112**, 13114 (2008).
- ⁸⁵ B.J. Skinner, R.C. Erd, and F.S. Grimaldi, *Am. Mineral.* **49**, 543 (1964).
- ⁸⁶ G. Brostigen and A. Kjekshus, *Acta Chem. Scand.* **23**, 2186 (1969).
- ⁸⁷ M. Lindqvist, D. Lindqvist, and A. Westgren, *Svensk Kemisk Tidskrift* **48**, 156 (1936).
- ⁸⁸ D. Lundqvist and A. Westgren, *Z. Anorg. Allg. Chem.* **239**, 85 (1938).
- ⁸⁹ E. Nowack, D. Schwarzenbach, and T. Hahn, *Acta Crystallogr. B* **47**, 650 (1991).
- ⁹⁰ A. Westgren, *Z. Anorg. Allg. Chem.* **239**, 82 (1938).
- ⁹¹ J. Trahan, R.G. Goodrich, and S.F. Watkins, *Phys. Rev. B* **2**, 2859 (1970).
- ⁹² R.W.G. Wyckoff, *Structure of Crystals, 2nd Ed.*, The Chemical Catalog Company, INC (1930).
- ⁹³ E. Nowack, D. Schwarzenbach, W. Gonschorek, and T. Hahn, *Z. Kristallogr.* **186**, 213 (1989).
- ⁹⁴ F.J. Mompean and M. Illemassène and J. Perrone, *Volume 6 of Chemical Thermodynamics: Chemical Thermodynamics of Nickel*, Elsevier (2006).
- ⁹⁵ H.E. King and C.T. Prewitt, *Am. Mineral.* **64**, 1265 (1979).
- ⁹⁶ H.T. Evans and J.A. Konnert, *Am. Mineral.* **61**, 996 (1976).
- ⁹⁷ E.H. Kisi and M.M. Elcombe, *Acta Crystallogr. C* **45**, 1867 (1989).
- ⁹⁸ G. Baldinozzi, J.-F. Berar, and G. Calvarin, *Mater. Sci. Forum* **278**, 680 (1998).
- ⁹⁹ K.R. Whittle, S.E. Ashbrook, and G.R. Lumpkin, *J. Solid State Chem.* **179**, 512 (2006).
- ¹⁰⁰ P. Bouvier, A.J. Dianoux, E. Djurado, G. Lucazeau, and C. Ritter, *Int. J. Inorg. Mater.* **3**, 647 (2001).
- ¹⁰¹ U. Martin, H. Boysen, and F. Frey, *Acta Crystallogr. B* **49**, 403 (1993).
- ¹⁰² G. Brauer, *Naturwissenschaften* **28**, 30 (1940).
- ¹⁰³ R. Pynn and J.D. Axe and R. Thomas, *Phys. Rev. B* **13**, 2965 (1976).
- ¹⁰⁴ W. Martin, R. Gruehn, and S. Andersson, *J. Solid State Chem.* **1**, 419 (1970).
- ¹⁰⁵ R.W.G. Wyckoff, *Crystal Structures* **1**, 85 (1963).
- ¹⁰⁶ G. Andersson and A. Magnéli, *Acta Chem. Scand.* **4**, 793 (1950).
- ¹⁰⁷ E.E. Rodriguez, F. Poineau, A. Llobet, A.P. Sattelberger, J. Bhattacharjee, U.V. Waghmare, T. Hartmann, and A.K. Cheetham, *J. Am. Chem. Soc.* **129**, 10244 (2007).
- ¹⁰⁸ J.A. Rard, G. Anderegg, H. Wanner and M.H. Rand, *Chemical thermodynamics of technetium*, North Holland, (1999).
- ¹⁰⁹ B. Krebs, *Z. Anorg. Allg. Chem.* **380**, 146 (1971).
- ¹¹⁰ A.A. Bolzan, C. Fong, B.J. Kennedy, and C.J. Howard, *Acta Crystallogr. B* **53**, 373 (1997).
- ¹¹¹ J.W.M. Biesterbos and J. Hornstra, *Journal of the Less-Common Metals* **30**, 121 (1973).
- ¹¹² J. Waser, H.A. Levy, and S.W. Peterson, *Acta Crystallogr.* **6**, 661 (1953).
- ¹¹³ P. Norby, R. Dinnebier, and A.N. Fitch, *Inorg. Chem.* **41**, 3628 (2002).
- ¹¹⁴ H.P. Walmsley, *Proc. Phys. Soc.* **40**, 7 (1928).
- ¹¹⁵ T. Schleid, *Eur. J. Solid State Inorg. Chem.* **29**, 1015 (1992).
- ¹¹⁶ F.J. Mompean, M. Illemassène and J. Perrone, *Volume 8 of Chemical Thermodynamics: Chemical Thermodynamics of Zirconium*, Gulf Professional Publishing (2005).
- ¹¹⁷ S. Furuseth, L. Brattas, and A. Kjekshus, *Acta Chem. Scand.* **29a**, 623 (1975).
- ¹¹⁸ N. Schoenberg, *Acta Metall.* **2**, 427 (1954).
- ¹¹⁹ H.A. Graf, A. Lerf, and R. Schoellhorn, *Journal of the Less-Common Metals* **55**, 213 (1977).
- ¹²⁰ C.J. Carmalt, T.D. Manning, I.P. Parkin, E.S. Peters, and A.L. Hector, *J. Mater. Chem.* **14**, 290 (2004).
- ¹²¹ R. de Jonge, T.J.A. Popma, G.A. Wiegiers, and F. Jellinek, *J. Solid State Chem.* **2**, 188 (1970).
- ¹²² V. Petkov, S.J.L. Billinge, P. Larson, S.D. Mahanti, K.K. Rangan, T. Vogt, and M.G. Kanatzidis, *Phys. Rev. B* **65**, 092105 (2002).
- ¹²³ K. Schwochau, *Technitium: Chemistry and radiopharmaceutical applications*, Wiley (2000).
- ¹²⁴ H.D. Lutz, B. Muller, T. Schmidt, and T. Stingl, *Acta Crystallogr. C* **46**, 2003 (1990).
- ¹²⁵ C.J. Stanley, A.J. Criddle, J. Spratt, A.C. Roberts, J.T. Szymanski, and M.D. Welch, *Mineral. Mag.* **69**, 447 (2005).
- ¹²⁶ E. Parthe, D. Hohnke, and F. Hulliger, *Acta Crystallogr.* **23**, 823 (1967).
- ¹²⁷ L. Thomassen, *Z. Phys. Chem. Abt. B* **4**, 277 (1929).
- ¹²⁸ F. Gronvold and E. Rost, *Acta Crystallogr.* **15**, 11 (1962).
- ¹²⁹ N.E. Brese, P.J. Squattrito, and J.A. Ibers, *Acta Crystallogr. C* **41**, 1829 (1985).
- ¹³⁰ F. Gronvold and E. Rost, *Acta Crystallogr.* **10**, 329 (1957).
- ¹³¹ G. A. Wiegiers, *Am. Mineral.* **56**, 1882 (1971).

- ¹³² P. Aldebert and J.P. Traverse, *Mater. Res. Bull.* **14**, 303 (1979).
- ¹³³ R. Ruh and P.W.R. Corfield, *J. Am. Cer. Soc.* **53**, 126 (1970).
- ¹³⁴ L.A. Aleshina and S.V. Loginova, *Kristallografiya* **47**, 460 (2002).
- ¹³⁵ M. Lamire, P. Labbe, M. Goreaud, and B. Raveau, *Rev. Chim. Minér.* **24**, 369 (1987).
- ¹³⁶ E. Salje, *Acta Crystallogr. B* **33**, 574 (1977).
- ¹³⁷ K. Meisel, *Z. Anorg. Allg. Chem.* **207**, 121 (1932).
- ¹³⁸ B. Krebs, A. Mueller, and H.H. Beyer, *Inorg. Chem* **8**, 436 (1969).
- ¹³⁹ V.M. Goldschmidt, *Skrifter utgitt av det Norske Videnskaps-Akademi i Oslo 1: Matematisk-Naturvidenskapelig Klasse* (1926).
- ¹⁴⁰ A. Zalkin and D.H. Templeton, *Acta Crystallogr.* **6**, 106 (1967).
- ¹⁴¹ A.A. Bolzan, C. Fong, B.J. Kennedy, and C.J. Howard, *Acta Crystallogr. B* **53**, 373 (1997).
- ¹⁴² J. Kumar and R. Saxena, *Journal of the Less-Common Metals* **147**, 59 (1989).
- ¹⁴³ Y. Nagano, *J. Therm. Anal. Calorim.* **69**, 831D839 (2002).
- ¹⁴⁴ E.E. Galloni and A.R. Roffo jr., *J. Chem. Phys.* **9**, 875 (1941).
- ¹⁴⁵ G.V. Samsonov, *The Oxide Handbook, 2nd Ed.*, Plenum Publishing Corporation, New York, (1982).
- ¹⁴⁶ O. Muller and R. Roy, *Journal of the Less-Common Metals* **16**, 129 (1968).
- ¹⁴⁷ G.M. Sheldrick, P.G. Jones, E. Schwarzmman, and H. Rumpel, *Acta Crystallogr. B* **35**, 1435 (1979).
- ¹⁴⁸ K. Aurivillius, *Acta Chem. Scand.* **18**, 1305 (1964).
- ¹⁴⁹ V.I. Marchenko and G.V. Samsonov, *Phys. Met. Metallogr.* **15**, 131 (1963).
- ¹⁵⁰ P. Basancon, P. Laruelle, J. Flahaut, and C. Adolphe, *Mater. Res. Bull.* **4**, 227 (1969).
- ¹⁵¹ J. D. D. Carre and M. Guittard, *Acta Crystallogr. B* **34**, 403 (1978).
- ¹⁵² K. Xu, Z. Wang, F. Wang, Y. Huang, F. Wang, L. Yin, C. Jiang, and J. He, *Adv. Mater.* **27**, 7881 (2015).
- ¹⁵³ A. Meetsma, G.A. Wiegers, R.J. Haange, and J.L. de Boer, *Acta Crystallogr. C* **46**, 1598 (1990).
- ¹⁵⁴ A. Meerschaut, L. Guemas, and J. Rouxel, *J. Solid State Chem.* **36**, 118 (1981).
- ¹⁵⁵ W.J. Schutte, J.L. de Boer, and F. Jellinek, *J. Solid State Chem.* **70**, 207 (1987).
- ¹⁵⁶ J.C. Wildervanck and F. Jellinek, *Journal of the Less-Common Metals* **24**, 73 (1971).
- ¹⁵⁷ T. Stingl, B. Muller, and H.D. Lutz, *Z. Kristallogr.* **202**, 161 (1992).
- ¹⁵⁸ S. Jovic, M.G.B. Drew, P. Deniard, J. Rouxel, R. Brec, and W.I.F. David, *J. Solid State Chem.* **89**, 315 (1990).
- ¹⁵⁹ F.A. Bannister and M.H. Hey, *Mineral. Mag.* **32**, 188 (1932).
- ¹⁶⁰ F. Groenvold, A. Kjekshus, and H. Haraldsen, *Acta Chem. Scand.* **14**, 1879 (1960).
- ¹⁶¹ T. Isonaga, K. Ishikawa, S. Wakita, and Y. Suzuki, *Solid State Ion.* **79**, 60 (1995).
- ¹⁶² H.E. Buckley and W.S. Vernon, *Mineral. Mag.* **20**, 382 (1925).